Ultralow-temperature ultrafast synthesis of wafer-scale single-crystalline graphene via metal-assisted graphitization of silicon-carbide

Se H. Kim[1,†], Hanjoo Lee[1,†], Dong Gwan Kim[2,†], Donghan Kim[3,†], Seugki Kim[4], Hyunho Yang[1], Yunsu Jang[1], Jangho Yoon[1], Hyunsoo Kim[5], Seoyong Ha[5], ByoungTak Lee[6], Jung-Hee Lee[6], Roy Byung Kyu Chung[2], Hongsik Park[3*], Sungkyu Kim[4*], Tae Hoon Lee[2*], Hyun S. Kum[1*]

[1]Department of Electrical and Electronic Engineering, Yonsei University, Seoul, South Korea
[2]Department of Advanced Materials Science and Engineering, Kyungpook National University, Daegu, South Korea
[3]Department of Electronic and Electrical Engineering, Kyungpook National University, Daegu, South Korea
[4]Department of Nanotechnology and Advanced Materials Engineering, Sejong University, Seoul, South Korea
[5]LX Semicon Co., Ltd., 222, Techno 2-ro, Yuseong-gu, Daejeon, South Korea
[6]L&D Co., Ltd., 179, Daehak-ro, Yuseong-gu, Daejeon, South Korea

* Indicates corresponding authors
† These authors contributed equally: Se H. Kim, Hanjoo Lee, Dong Gwan Kim, Donghan Kim

* Corresponding author: Hongsik Park, Sungkyu Kim, Tae Hoon Lee, Hyun S. Kum
* E-mail address: hpark@ee.knu.ac.kr, sungkyu@sejong.ac.kr, thl@knu.ac.kr, hkum@yonsei.ac.kr

Abstract

Non-conventional epitaxial techniques, such as van der Waals epitaxy (vdWE) and remote epitaxy, have attracted substantial attention in the semiconductor research community for their exceptional capability to continuously produce high-quality free-standing films on a single mother wafer without needing surface refurbishment. The successful implementation of these emerging epitaxial techniques crucially hinges on creating a robust uniform two-dimensional (2D) material surface at the wafer-scale and with atomically precise uniformity. The conventional method for fabricating graphene on a silicon carbide (SiC) wafer is through high-temperature graphitization, which produces epitaxial graphene on the surface of the SiC wafer. However, the extremely high temperature needed for silicon sublimation (typically above 1500°C) causes step-bunching of the SiC surface in addition to the growth of uneven graphene at the edges of the step, leading to multilayer graphene stripes and unfavorable surface morphology for epitaxial growth. Here, we fully develop a graphitization technique that allows fast synthesis of single-crystalline graphene at ultra-low temperatures (growth time of less than 1 minute and growth temperature of less than 500°C) at wafer-scale by metal-assisted graphitization (MAG). We found annealing conditions that enable SiC dissociation while avoiding silicide formation, which produces single-crystalline graphene while maintaining atomically smooth surface morphology. The thickness of the graphene layer can be precisely controlled by varying the metal thickness or annealing temperature, allowing the substrate to be utilized for either a remote epitaxial growth substrate or a vdWE growth substrate, depending on the thickness of the graphene. We successfully produce freestanding single-crystalline ultra-wide bandgap (AlN, GaN) films on graphene/SiC via the 2D material-based layer transfer (2DLT) technique. The exfoliated films exhibit high crystallinity and low defect densities. Our results show that low-temperature graphene synthesis via MAG represents a promising route for the commercialization of the 2D-based epitaxy technique, enabling the production of large-scale ultra-wide bandgap free-standing crystalline membranes.

Keywords: Graphitization; Ultra-wide bandgap; van der Waals epitaxy; Remote Epitaxy; 2D-coated substrate; Graphene

1. Introduction

Two-dimensional (2D) material-based epitaxy techniques, such as van der Waals epitaxy (vdWE) and remote epitaxy, have recently garnered substantial attention due to their ability to address fundamental challenges inherent in conventional heteroepitaxial techniques caused by lattice and thermal expansion mismatches[1–5]. The vdWE and remote epitaxial techniques not only alleviate these issues, but also potentially allow reuse of costly semiconductor substrates for significant cost reduction of electrical devices. These techniques enable precise exfoliation of highly functional single-crystalline membranes and allow heterogeneous integration of dissimilar materials, thereby enabling the integration of distinct electronic and photonic elements onto a single platform[1]. Numerous studies on these epitaxial techniques have been investigated for various semiconductors (Si, Ge, III-V, and III-nitride materials) as well as complex oxides (perovskites, spinels, and garnets)[2–4,6–8]. Successful use of graphitized silicon carbide (SiC) substrates for remote and vdW epitaxy of GaN membranes has also been demonstrated recently[4,8]. Single-crystalline SiC is one of the most promising candidates for remote and vdW epitaxial growth due to its ability to form uniform defect-free and atomically flat graphene at wafer-scale through high-temperature graphitization. The graphitization process eliminates the need to transfer graphene onto the host substrate for growth, preventing process-induced damage or residues on the graphene layer that can hinder the growth of high-quality epitaxial films. However, graphitization and subsequent formation of graphene on SiC usually occurs at very high temperatures that exceed 1500°C[9,10]. This high-temperature requirement is a technical obstacle as the high temperature not only causes significant step-bunching of the SiC surface but also leads to non-uniform growth of graphene at the edges of the step[9].

Recently, several groups have reported on a new graphitization method of SiC substrates utilizing thin metal films as a catalyst to reduce the temperature of graphitization. This metal-assisted graphitization (MAG) process can be achieved through the deposition of various metals on the SiC substrate, such as nickel (Ni), iron (Fe), ruthenium (Ru), cobalt (Co) and its alloys[11–21]. These studies showcase the catalytic effect of metals in breaking the Si-C covalent bond at temperatures below 1100°C. However, a few groups have identified defective interface graphene at the metal-silicide/SiC substrate[15–19], suggesting that liberated carbon atoms diffuse inside the metal-silicide layer in the annealing process, which then precipitates at the

silicide/SiC interface to form graphene in the cooling process. Unfortunately, the reaction between the metal and dissociated Si atoms leading to silicide formation appears to be dominant[13,16] , which not only deteriorates the uniformity and roughness of graphene[13,18] but also causes surface damage to the SiC substrate[15,17]. Notably, Lim et al. reported that SiC decomposes at approximately 450°C using Ni as the catalyst, even below the silicide formation temperatures, resulting in the formation of 6~8 nm multilayer graphene at the metal/SiC interface due to the differences in the solubility of carbon and silicon in Ni[19]. However, the formation mechanism and properties of the interface graphene synthesized by MAG remain unclear due to limited information on surface morphology, domain size, and graphene uniformity as previous studies have predominantly focused on graphene formed on reacted metal surfaces, silicide surfaces, and silicide/SiC interface. Thus, further investigation is needed to bridge this knowledge gap.

Here, we demonstrate ultra-fast growth of wafer-scale graphene on a 4-inch SiC substrate below 500°C, with precise control on the number of graphene layers by changing the metal thickness and annealing temperature. The resulting graphene grown by MAG exhibits overall uniform characteristics comparable to graphene synthesized by traditional high-temperature graphitization. Moreover, the III-nitride films grown on MAG-treated SiC via 2D-assisted epitaxy demonstrate quality comparable to those grown on high-temperature graphitized SiC and conventional substrates such as sapphire and SiC via MOCVD. These breakthroughs hold significant promises for advancing semiconductor technologies using SiC as epitaxial substrates. To gain a comprehensive understanding of the MAG mechanism and its applicability, we carried out the catalyst effects of various metal elements such as Ni, Fe, and Ru. Our results offer valuable insights into the general mechanisms of the MAG process, providing a more accessible approach for synthesizing wafer-scale graphene which can be readily used as remote or vdW epitaxial substrates.

2. Results and discussion

Metal-assisted graphitization (MAG) of SiC was first reported by Juang et al.[11], in which they studied the formation of graphene by depositing a thin Ni layer on SiC and annealing at relatively low temperatures. They found that the metal film acts as a decomposition catalyst above a certain temperature (> 700°C), which is sufficient to fully overcome the activation barrier for silicide formation. The tendency of metal to react with Si reduces the Si-C bonding

energy, thereby lowering the temperature required for Si sublimation and subsequent graphitization of the SiC. We carried out a meticulous study by varying the catalyst metal element and annealing temperature as well as performing DFT calculations to fully understand the MAG process on SiC. The process of MAG is illustrated in Fig 1a (see Supplementary Fig. 1 for details of the 4-inch wafer MAG process). A thin layer of metal is deposited onto a 4º off-axis 4H-SiC (0001) substrate using sputtering or e-beam evaporation for Ni, Ru, and Fe, followed by annealing in a rapid thermal annealing (RTA) chamber. After cooling, any residual metal film is etched away in its respective etchants. A photograph of the resulting graphitized SiC, prepared with the appropriate metal, is shown in Fig 1b. The graphitized sample shows a weak visible-light absorption, as indicated by the ultraviolet-visible (UV-vis) transmittance spectra (see Supplementary Fig. 2). Fig 1c illustrates a possible mechanism describing how carbon atoms redistribute in the presence of metal catalysts at elevated temperatures, forming a graphene layer at the metal-SiC interface. The MAG process is characterized by three distinct stages. In Stage 1, once sufficient thermal energy is introduced, the metal catalyst facilitates the decomposition of Si–C bonds. In Stage 2, as the annealing temperature increases, further dissociation occurs. The system then stabilizes as newly released C atoms either migrate outward into the metal bulk (i) or remain at the metal/SiC interface to form graphitic carbon or graphene layers (ii or iii). The redistribution of C atoms likely varies significantly depending on the type of metal, possibly due to differences in solubility and chemical affinity. Stable graphene layers are expected to form at the metal/SiC interface as a final product of the interactions (Stage 3), but only when appropriate metals are used.

To understand the MAG processes proposed in Fig 1c, it is crucial to first examine the microscopic mechanism of metal-assisted graphitization of SiC. Previous studies indicate that the dissociation of SiC is driven by its reaction with metals to form thermodynamically favored metal-silicides[22–24]. Ni, Ru, and Fe, which exhibit highly negative enthalpies of silicide formation[25], enable dissociation at lower temperatures compared to the conventional graphitization process. However, the distinct properties of each metal, such as the solubility of silicon and carbon in the metal and their chemical affinity with the metal, may significantly influence not only the distribution of silicon and carbon within the metal but also the interaction of the metal with SiC or graphene. As a result, significantly different behaviors during Stages 2 and 3 are expected depending on the metal catalyst utilized, which has not been thoroughly investigated. Additionally, most previous MAG studies primarily focused on carbon

distribution after the metal had converted into silicide, where precipitated carbon was observed at both the silicide/SiC interface and the silicide surface due to the solubility limitations of carbon during the cooling stage. These approaches, however, overlooked the distribution of C and Si immediately after the Si-C bond dissociation in the initial stage, where the effect of the metal is assumed to be most significant. This lack of knowledge regarding the early stage of carbon redistribution in the MAG process has resulted in outputs unsuitable for device applications due to challenges such as uneven SiC consumption[16] and graphene clustering[13], both attributed to localized silicide formation[15,17,18].

To bridge the gap in understanding the microscopic processes at the early stage of the MAG process, as well as to elucidate the metal-specific differences, we employed *ab initio* molecular-dynamics (AIMD) simulations. We considered three metal elements-Ni, Ru, and Fe-as catalysts and investigated the initial stage of carbon redistribution following Si-C bond dissociation to unveil the dependence of stable graphene formation on metal types (see Supplementary Note 1 and Supplementary Fig. 3 and 4 for detailed simulation methods). Fig 1d shows the structural evolution of carbon atoms at the metal-SiC interface during AIMD simulations. Interesting observations include: (i) carbon and metal atoms tend to diffuse into each other to a certain extent at the metal-SiC interface, resulting in slight intermixing between the carbon and metal elements (Stage 2); (ii) carbon atoms in the graphene layer maintain their hexagonal arrangement, with the degree of structural order depending on the metal type. The evolution of the number of six-fold rings in the graphene layer and carbon atoms with three-fold coordination indicates that Ni is the most effective in stabilizing the graphene layer (Stages 2 and 3), while significant disordering occurs with the other metals (see Supplementary Video 1-3 (redacted for arXiv submission); and (iii) the van der Waals gap between the metal and graphene layer is relatively well maintained in the Ni-containing model (Stage 3), whereas Fe- or Ru-containing models show a collapse of the gap (Supplementary Fig. 6). These AIMD results highlight the distinctive catalytic role of the Si-dissolved Ni matrix in driving carbon reorganization and graphene-like structure formation. Ni, known for its high silicon solubility[26] and low carbon affinity[22], facilitates graphene formation at the metal/SiC interface. In contrast, graphene layers become unstable with Ru, (low Si solubility[27]) and Fe (high carbon affinity[28]), emphasizing the importance of selecting a catalytic metal with high Si solubility and low carbon chemical affinity.

These DFT results align well with our experimental results, demonstrating that only Ni enables the formation of uniform graphene at the metal/SiC interface without any silicide formation. A schematic representation of the metal's effect on MAG, highlighting the significant differences in outcomes, is illustrated in Fig 2a. To experimentally verify the catalyst effect of each metal in reducing the Si-C dissociation barrier energy during the MAG process, we measured X-ray photoelectron spectroscopy (XPS) C 1s and Si 2p spectra after annealing at significantly low temperature (Supplementary Fig. 7). The liberation of C and Si atoms was observed when annealing the samples at 500°C for Ni and Fe, and at 400°C for Ru, showcasing a significant reduction in the energy required for Si-C bond dissociation. The formation of carbon layers on the metal surface, produced either by dissociated carbon diffusing through grain boundaries[21] or due to the low solubility of carbon in the metal matrix[20], was further confirmed by Raman spectroscopy, supporting the XPS results (Supplementary Fig. 8). After confirming Si-C bond dissociation in all metal/SiC systems, we investigated the temperature-dependent phase transformations in the metals, including the formation of silicide through solid-state reactions. As shown in Fig 2b, no silicide peaks were detected for Ni annealed at 500°C, and Fe annealed at 400°C, even though the liberated Si atoms were observed in the XPS Si 2p spectra (Supplementary Fig. 8). However, at higher temperatures, an upshift in binding energy was observed, 0.3 eV for Ni and 0.5 eV for Fe, indicating the formation of Ni_2Si and $Ni_{31}Si_{12}$ mixed phases[29], and FeSi[30]. For Ru, a shift in binding energy (0.3 eV) was already evident at 350°C, indicating the formation of Ru_2Si_3[31]. These solid-state reactions of metal/SiC were further supported by X-ray diffraction (XRD) measurements (Supplementary Fig. 9). Due to the overlap of C 1s spectra with Ru 3d spectra in XPS and indistinguishable peaks in XRD scans, Raman spectra were further employed for supporting structural change (Supplementary Fig. 10). We further observed distinct effects of each metal on graphene formed at the metal surface. A distinct 2D peak in Raman spectra was only detected on Ni without the formation of a silicide layer (Supplementary Fig. 11). For Fe, graphene formation occurred only after silicide formation, where liberated carbon atoms were either contained within the metal or distributed at the metal/SiC interface. In contrast, Ru did not form a graphene layer but an amorphous carbon layer below 400°C, despite the silicide reaction having already proceeded, potentially indicating a need for higher temperatures to crystallize the carbon layer into graphene[11,16].

Since DFT calculations indicated significant differences in the possibility of graphene formation at the interface of each metal/SiC depending on the metal, further investigations of

the metal/SiC interface were conducted. The residual metal film was etched away using its respective etchant after annealing at the minimum temperature that confirmed Si-C dissociation. Raman spectra and the optical image (OM) confirmed that a graphene layer was synthesized on SiC only when Ni was used as the catalyst, as in agreement with DFT results (Supplementary Fig. 11). In contrast, no carbon layer was detected for Ru annealed at 350°C while an uneven amorphous carbon layer was observed for Fe annealed at 400°C, suggesting that the carbon at the metal/SiC interface either diffused outward into the reacted region or was absorbed into the metal layer without any reconstructing the amorphous carbon to graphene, as consistent with DFT results. These results unambiguously verify that the selection of the metal catalyst plays a crucial role in the MAG process. Among the metals studied, only the Ni enabled uniform, wafer-scale graphene formation at the metal/SiC interface without conversion of the metal into silicide or carbide phases during the MAG process.

After selecting the appropriate metal (Ni) based on the above results, further experimental studies were conducted to validate the carbon distribution model at both low temperatures (stage 1 in Fig 1c) and relatively high temperatures (stage 2 in Fig 1c). We further lowered the annealing temperature not only to control the thickness of the graphene but also to explore the relationship between annealing temperature and Si-C bond dissociation. As shown in Fig 2d and Supplementary Fig. 12, transmission electron microscopy (TEM) analysis confirmed the formation of 4-layer graphene at the Ni/SiC interface after annealing at 500°C for ~1 second, while mono-layer graphene formed at 320°C for ~1 second. Both results indicate that slightly thicker graphene was formed at the Ni surface than interface of Ni and SiC, the liberated C atoms tend to diffuse slightly more at the grain boundary in Ni rather than at the interface of Ni and SiC. These results are consistent with the UV-vis transmittance spectra obtained at the macroscopic scale after etching with a respective etchant (Supplementary Fig. 13). Furthermore, when the annealing temperature was increased to 550°C, we observed not only inhomogeneous silicide reactions but also clustering of graphene, as confirmed by atomic force microscopy (AFM), scanning electron microscopy (SEM), and Raman spectroscopy (Supplementary Fig. 14). These findings align with observations reported in the literatures[15,20]. Furthermore, we reduced the thickness of Ni from 50 nm to 8 nm to investigate the relationship between metal thickness and graphene thickness. As dissociated Si atoms are homogeneously distributed within the Ni lattice[32], we hypothesized that reducing the metal thickness would decrease the reactivity between SiC and Ni. This reduction is attributed to the lower gradient-driven

diffusion of Si atoms at thinner metal layers, resulting from shorter diffusion pathways or a diminished driving force for Si-C dissociations, thereby leading to thinner graphene on the SiC surface. As shown in Fig 2d, the thickness of graphene on the SiC surface decreased to approximately 1 monolayer (ML). These findings align with the UV-vis transmittance spectra measured at the macroscopic scale after etching with the respective etchant (see Supplementary Fig. 15). Overall, the results indicate that the MAG process is primarily temperature-driven, in agreement with the MAG carbon distribution model. Moreover, the thickness of the graphene layer on the SiC substrate can be precisely controlled by adjusting the metal layer thickness or the annealing temperature.

Next, we characterized the graphene layers formed on SiC by etching away the Ni layer graphitized at 500°C for ~1 second. The presence of graphene was confirmed by C 1s X-ray photoelectron spectroscopy (XPS), as shown in Fig 3a. In the spectra, the peak labeled SiC corresponds to the Si-C bonds in the SiC substrate. The components S1 and S2 are attributed to sp^2- and sp^3-hybridized carbon atoms, respectively. These peaks indicate the presence of a graphene layer (S1) and a carbon buffer layer (CBL) or sp^3-defective graphene (S2)[8]. Additionally, the XPS Ni 2p spectra and energy-dispersive X-ray spectroscopy (EDS) confirmed the complete removal of Ni, as it was not detected on the surface (Supplementary Fig. 16). The graphene was also characterized using plan-view TEM (See Experimental details). The TEM image along with the selected area electron diffraction (SAED) pattern reveals a well-aligned honeycomb lattice, providing clear evidence of single-crystalline graphene, as shown in Fig 3b. To evaluate the characteristics of graphene on a macroscopic scale, Raman spectroscopy was employed, as shown in Fig 3c. The Raman spectra confirmed the presence of a graphene layer through the characteristic D, G, and 2D bands. It also enabled the assessment of graphene thickness and quality by analyzing the 2D band full width at half maximum (FWHM). The FWHM of the 2D band serves as a reliable quantitative measure to distinguish the number of layers, ranging from single-layer graphene (typically, 27.5 ± 3.8 cm^{-1}) to four-layer graphene (typically, 63.1 ± 1.6 cm^{-1})[33]. To evaluate the macroscopic uniformity of graphene thickness, Raman mapping of the 2D band FWHM was performed, as shown in Fig 3d. The results demonstrated consistent values across the sample, with a mean FWHM of 60 cm^{-1} and a standard error of 0.059, indicating uniform 4 ML graphene across the entire area. These results are consistent with the TEM images and UV-vis spectra, as shown in Fig 2d and Supplementary Fig. 13, respectively. Furthermore, the positions of G and 2D bands provide

valuable insights into graphene quality, thickness, strain effects and other characteristics[34]. As shown in Fig 3e and Fig 3f, the average calculated G band position was 1580 cm^{-1} with a standard error of 0.52, while the average calculated 2D band position was 2690 cm^{-1} with a standard error of 0.18. These results confirm not only the uniform properties but also the consistent graphene thickness across the entire SiC substrate. Furthermore, complete graphene coverage across the 4-inch SiC substrate was confirmed (see Raman spectra and camera image in Supplementary Fig. 17), demonstrating the capability to produce 4-inch graphene directly on a semiconductor substrate using a very low-temperature, ultra-fast process, that relies solely on RTA and sputtering, which are techniques fully compatible with Si CMOS industry standards.

The results of MAG suggest that the SiC substrate can be used as an ideal substrate for producing single-crystalline free-standing high-quality III-nitride films via remote epitaxy and vdWE by controlling the thickness of graphene through modifying the annealing temperature. Remote epitaxy is an advanced epitaxial technique where epitaxial growth occurs on a substrate covered with a 2D material[1]. The partial transparency of the 2D layer to Coulombic interactions allows adatoms to electrostatically interact with the underlying substrate[1–3]. At the substrate-epitaxial membrane interface, the 2D material and its van der Waals gap effectively eliminate dislocations or cracks in the epitaxial membrane caused by lattice strain relaxation, which has been a persistent challenge in conventional techniques for achieving high-quality epitaxial devices[2,35,36]. In contrast, vdWE involves epitaxial growth on surfaces without dangling bonds, such as 2D materials, or on 3D materials with passivated dangling bonds. These slippery interfaces enable strain relaxation, allowing the growth of materials with significant lattice mismatches greater than 60%[1]. Furthermore, in both 2D-based epitaxial techniques, epitaxial membranes are bound to the 2D material via weak van der Waals interactions. This characteristic enables the fabrication of free-standing membranes through 2D material-assisted layer transfer (2DLT)[7]. These approaches are particularly advantageous, as they allow the repeated reuse of expensive substrates while producing multiple single-crystalline membranes. A schematic of the detailed 2D-based epitaxy and 2DLT process is shown in Supplementary Fig. 18.

III-nitrides, such as GaN and AlN, are promising candidates for high-temperature logic and power devices as well as light emitting diodes due to their exceptional intrinsic material

properties[37,38]. These include wide direct bandgaps (3.4 eV for GaN and 6.2 eV for AlN)[38,39], high breakdown electric field (4.9 MV cm^{-1} for GaN and 15.4 MV cm^{-1} for AlN)[47], and high electron mobility. These materials are particularly well-suited for 2D-based epitaxial growth on graphitized SiC, as their hexagonal lattice arrangement aligns well with SiC, enabling the formation of single-crystalline membranes via remote epitaxy. Furthermore, the graphitization of SiC produces nearly pristine graphene, whose preserved hexagonal lattice structure enhances the growth of c-plane III-nitrides films, offering significant benefits for vdWE[36]. Finally, the direct synthesis of graphene on SiC eliminates the need for wet-transferred graphene synthesized on metal foils via CVD, which often introduces defects such as wrinkles, holes, interfacial contamination, and organic residues. These defects can disrupt the remote interaction between the substrate and the remote epitaxial film, as well as between the graphene and the van der Waals epitaxial film[2].

Although the advantages of the graphitized SiC template for 2D-based epitaxy are clear, high-quality III-N membrane growth on graphene faces challenges due to its low chemical reactivity[40]. The high surface migration rate of group III metals on slippery graphene prevents nuclei from stabilizing at their original positions, mitigating the formation of high-density boundaries and defects. However, this also results in epitaxial failure due to insufficient nucleation sites[36]. High-quality single-crystalline AlN film growth via vdWE on graphitized SiC has been reported, where plasma treatment was applied to the graphitized SiC to enhance nucleation by introducing defects on the graphene surface[36,41]. However, the exfoliation of the resulting layers was not demonstrated, as the focus was on synthesizing crack-free AlN layers that leveraged the stress relaxation benefits of graphene. Since the membrane exfoliation yield via 2DLT improves with a uniform graphene layer covering the entire surface on the substrate, untreated graphene is required to successfully produce freestanding membranes. The successful exfoliation of high-quality single-crystalline GaN on non-defect-induced graphitized SiC via 2D-assisted epitaxy was first reported in 2014, achieved not only by engineering the epitaxial growth strategy on a 2D surface but also by utilizing the periodical step edges of SiC[4]. These step edges, with terrace widths typically ranging from 5 to 10 μm and step heights from 10 to 15 nm[4,41], remain after the step bunching induced by high-temperature processes[42]. These periodic step edges generate uniform fluctuations in electric potential, providing energetically favorable nucleation sites for adatoms and enabling the growth of single-crystalline GaN[4]. In this regard, our MAG-graphitized approach is expected to offer significant advantages since

the MAG process is conducted at low temperatures, which avoids step bunching and preserves the naturally periodic small terraces of 4° offcut 4H-SiC. The terraces have widths of under 7.2 nm and step heights of under 0.5 nm[43], as illustrated in Fig 4a.

As predicted, we were able to successfully grow high-quality AlN films on both 4 ML graphene/SiC via vdWE and 1 ML graphene/SiC via remote epitaxy. For both samples, electron backscatter diffraction (EBSD) maps with SEM images and XRD scans confirmed a (002) wurtzite orientation across a large area, as shown in Fig 4b and Fig 4c. These results indicate that single-crystalline AlN can be grown via remote epitaxial seeding from 1 ML graphene/SiC and van der Waals epitaxial seeding from 4 ML graphene/SiC (see the illustrated image in Supplementary Fig. 19). However, the FWHM of AlN (002) peaks in XRD scans broadened with increasing graphene thickness on SiC, suggesting lower seeding efficiency compared to remote epitaxy. A prior study reported the successful exfoliation of high-quality AlN on graphitized SiC grown via 2D-based epitaxy, achieving an AlN (002) FWHM of 3600 arcsec at a thickness of 670 nm[40]. In contrast, our study demonstrated significantly improved quality on MAG-treated SiC, with remote epitaxy achieving an AlN (002) FWHM of 673 arcsec at a thickness of 270 nm and vdWE-grown AlN exhibiting an AlN (002) FWHM of 1890 arcsec at a thickness of 285 nm (see cross-sectional SEM images in Supplementary Fig. 20). To compare the MAG sample with the conventional graphitized sample, we conducted high-temperature graphitization process (see experimental details). Our sample exhibited step bunching along with a graphene layer, consistent with findings from previous research (see Raman spectra with AFM image in Supplementary Fig. 21). We performed AlN growth under identical conditions following graphitization at high temperature. As shown in Fig 4d, SEM images reveal that AlN adatoms preferentially nucleate at the SiC step edges, whereas a polycrystalline nature of AlN was observed on the SiC terraces. We concluded that the dramatically enhanced crystallinity of AlN can be attributed to the presence of tightly packed and periodically stepped SiC, as shown in the TEM images in Fig 2d and Fig 2e. These features provide highly energetically favorable nucleation sites, which are effective for both remote epitaxy[4] and vdWE[36,44].

After confirming the successful growth of a single-crystalline AlN layer on MAG-treated SiC, we used it as a buffer layer to grow a single-crystalline GaN. In conventional epitaxy, AlN layers (a-axis: 3.112 Å) are commonly employed as intermediate layers to address the lattice mismatch between GaN (a-axis: 3.189 Å) and SiC (a-axis: 3.073 Å), thereby enhancing the

quality of GaN. While graphene as a buffer layer effectively relaxes the lattice strain of GaN thin films, the crystallinity of GaN grown on AlN synthesized via 2D-assisted epitaxy still requires thorough investigation. To evaluate this, we grew GaN on each 2D-assisted epitaxial AlN templates and conducted XRD and EBSD measurements to determine the crystallinity on a macroscopic scale. The EBSD maps with SEM images and XRD scans verified the (002) wurtzite orientation over a large area, indicating single crystallinity of the grown GaN film on both AlN templates, as shown in Fig 4e and Fig 4f. Notably, the FWHM of GaN (002) on XRD scans ranges from 385 arcsec to 496 arcsec, showing no variation based on the choice of AlN template. These results are comparable not only to those of AlN-buffer-assisted GaN films on conventional substrates such as sapphire or SiC via MOCVD, but also to the remote epitaxial growth of GaN on graphitized SiC (see Supplementary Table 1). After confirming the single crystallinity of the GaN layer, we utilized 2DLT to exfoliate both samples. Following the deposition of the adhesion layer (Ti) and stressor layer (Ni) on the surface of GaN samples, mechanical exfoliation was carried out using thermal release tape (TRT) as a handling layer. The strain energy generated by the Ni stressor guided crack propagation precisely along the AlN/graphene interface, facilitated by the weak van der Waals bonds between the GaN/AlN and the graphitized SiC. As a result, freestanding GaN/AlN membranes were successfully obtained using both MAG-treated templates (see Supplementary Fig. 22). All these results highlight the advantages of MAG-treated SiC templates, suggesting their potential as a future method for producing the freestanding ultra-wide bandgap III-nitrides materials. Our approach not only dramatically reduces the barrier of preparing epitaxial graphene coated single-crystalline substrates, but also significantly enhances the crystallinity of the freestanding single-crystalline membranes for heterogeneous integration.

4. Conclusions

In conclusion, we have investigated and identified the most optimal condition for ultralow temperature ultrafast graphitization of SiC. Our findings demonstrate that the metal employed significantly influences the presence of graphene layers on SiC, with Ni being the only catalyst capable of synthesizing uniform graphene on SiC. These findings underscore the importance of selecting appropriate metals to facilitate graphene growth while minimizing undesired reactions, thus contributing to the optimization of graphene synthesis processes for various applications. Our study successfully demonstrates not only the growth of a continuous

graphene layer on a 4-inch SiC wafer at low temperature with an ultra-fast process but also the reproducible synthesis of the free-standing single-crystalline membrane through 2D-based epitaxy. This significant breakthrough facilitates the 3D heterogeneous integration of dissimilar materials, paving the way for the seamless integration of distinct electronic and photonic elements on a single wafer.

Experimental details

Computational details

The first-principles calculations were performed using the projected augmented wave (PAW) plane-wave basis, implemented in the Vienna ab initio simulation package (VASP)[45]. An energy cutoff of 520 eV was employed and the atomic positions were optimized using the conjugate gradient scheme without any symmetric restrictions, until the maximum force on each of them was less than 0.01 eV/Å[46]. All atoms were relaxed to their equilibrium positions when the change in energy on each atom between successive steps converged to 1×10^{-6} eV/-atom. The heterostructure was modeled with an 8×8×1 grid for k-point sampling. The generalized gradient approximation (GGA) exchange-correlation (XC) DFT functional Perdew-Burke-Ernzerhof (PBE) was employed for geometrical optimization and electronic structure calculations[47]. The slab models had dangling bonds on the vacuum surface terminated by pseudo-hydrogen atoms with appropriate fractional charges to avoid surface states. To determine the vacuum level, dipole corrections are introduced to compensate for the artificial dipole moment at the open ends (20 Å vacuum space along the c-axis) arising from the periodical boundary condition imposed in these calculations[48]. Ab initio molecular dynamics (AIMD) simulations were performed in supercells using DFT calculations with a gamma-centered k-point. The time step was set to 3 fs. Simulations for 3 ps were run with a time step of 3 fs to study the dynamic graphitization process. The temperature of the simulation system was controlled at 2273 K using the Nosé–Hoover thermostat[49,50].

Sample preparation

The single-crystalline 4° offcut 4H–SiC (0001) substrates were supplied by Cree, Inc.. To remove organic contaminants, substrates were cleaned sequentially for 5 min in acetone, 5 min Iso Propyl Alcohol in an ultrasound bath, and finally dried by nitrogen gun.

Metal deposition and graphene formation/transfer method

After preparing the SiC substrate, we deposited Ni, Fe, and Ru onto each SiC substrate to

investigate the effect of metal catalysts on the interface graphene layer. Ni was deposited on the substrate using a DC magnetron sputtering apparatus with an Ar plasma at room temperature (JURA deposition apparatus made by Vakuum Servis Ltd., Czech Republic). The sputtering was carried out in an Ar atmosphere (pressure 0.5 mTorr) with DC power 100 W. Resulting deposition rate was 2.5 nm/min. Fe and Ru were deposited on the substrate using an e-beam evaporator (Korea Vacuum Tech., Korea Republic). The base pressure was maintained below 5×10^{-7} torr, with a deposition rate of 0.6 Å/s.

Following metal deposition, the samples underwent rapid thermal annealing (RTA). The base pressure during RTA was maintained at 7×10^{-3} torr, with 1 torr of N_2 added to prevent metal oxidation. The samples were annealed for 3 minutes to determine the temperature required to decompose the Si-C bond and assess whether it induces a phase change of metals into silicide. X-ray photoelectron spectroscopy (XPS, K-alpha, Thermo Scientific Inc.) and X-ray diffraction (XRD, Rigaku, SmartLab) with Cukα1 (wavelength 1.54051 Å) were used to identify crystalline phases and structural transformations in the metal/SiC structure. Raman spectroscopy (Horiba Jobin Yvon, LabRam Aramis) equipped with a 532 nm wavelength laser was utilized to analyze phase transformations of metals and to confirm the presence of graphene. Following the reaction, the interfacial graphene layer was analyzed using high-resolution transmission electron microscopy (HRTEM, JEOL ARM200F). To further investigate the interface characteristics, the samples were immersed in a 40% w/v Ferric Chloride ($FeCl_3$) solution (for Ni, and Fe) for 5 minutes or a 5% w/v Sodium Hypochlorite (NaOCl) solution (for Ru) for 5 minutes. The samples were then characterized using optical microscopy (OM), scanning electron microscopy (SEM, JEOL, JSM-IT-500HR), Ultraviolet-visible-near-infrared spectrophotometer (UV-vis-NIR, JASCO, V-650), atomic force microscopy (AFM, Park Systems, NX-10), TEM, and Raman spectroscopy.

After graphene synthesis, polyvinyl alcohol (PVA) was drop-casted onto the surface and baked at 80°C for 5 minutes to form an adhesion layer. A TRT was then attached, facilitating the detachment of graphene through mechanical exfoliation. The exfoliated graphene was transferred onto an SiO_2 substrate. The TRT was removed by baking the sample at 130°C, and the graphene was revealed by dipping the sample into deionized water.

SiC high-temperature graphitization

The wafer was loaded into an Aixtron VP508 reactor for graphitization. It was first cleaned in a hydrogen environment for 30 minutes at 1520°C, followed by annealing at 1580°C in a

700 Torr argon ambient for 10 minutes.

III-N epitaxial Growth and exfoliation

The GaN/AlN hetero-structure was epitaxially grown on a graphene/SiC substrate by a metal-organic chemical vapor deposition (MOCVD) equipped with a vertical showerhead-type chamber from Sysnex Co., Ltd. The MOCVD reactor maintained a stable pressure of 30 Torr with hydrogen as a carrier gas throughout the growth process. Initially, the AlN buffer layer was grown at 1,050°C for 40 mins on 1 ML graphene/SiC and 4 ML graphene/SiC. Subsequently, GaN layer was grown by a single-step growth at 1,100 °C for 4 mins on each AlN layer. In this growth process, trimethylgallium, trimethylaluminum, and ammonia were used as the sources of gallium, aluminum, and nitrogen, respectively. The resulting GaN/AlN epilayers were exfoliated using a Ti/Ni stressor stack with a handling layer. A 50 nm thick Ti layer was deposited as an adhesion layer for the Ni stressor layer via e-beam evaporation, followed by the deposition of a 3.5 μm thick Ni stressor layer using DC magnetron sputtering under an argon ambient. After the deposition of Ti/Ni layers, thermal release tape (TRT) was attached as a handling layer. Finally, the TRT/Ti/Ni/epi stack was lifted from the edges, enabling precise and controlled exfoliation of the GaN/AlN epilayers.

III-N membrane characterizations

The plan-view, cross-sectional, and EBSD images of the grown and exfoliated samples were obtained using a field-emission SEM system (SU8220, Hitachi). X-ray diffraction characterization was carried out using an XRD measurement system with Cu K-α radiation (Empyrean, Malvern Panalytical).

Credit authorship contribution statement

Se H. Kim: Conceptualization, Writing – original draft, Visualization, Methodology, Investigation. **Hanjoo Lee:** Investigation, Writing – original draft. **Dong Gwan Kim:** DFT simulation, Writing – original draft. **Donghan Kim:** Investigation, Visualization, Validation. **Seugki Kim:** Visualization, Validation. **Hyunho Yang:** Visualization, Validation. **Yunsu Jang:** Visualization, Validation. **Jangho Yoon:** Validation. **Hyunsoo Kim:** Resources. **Seoyong Ha**: Resources. **ByuongTak Lee**: Resources. **Jung-Hee Lee**: Resources. **Roy Byung Kyu Chung**: Resources. **Hongsik Park:** Validation, Resources. **Sungkyu Kim:** Validation, Resources. **Taehoon Lee:** Validation, Resources. **Hyun S. Kum:** Conceptualization, Methodology, Investigation, Resources, Writing – review & editing, Project administration, Supervision.

Declaration of Competing Interest

The authors declare that they have no known competing financial interests or personal relationships that could have appeared to influence the work reported in this paper.

Data availability

Data will be made available on request.

Acknowledgments

The team at Yonsei University would like to acknowledge support from LX Semicon, the National Research Foundation of Korea (NRF) (grant no. RS-2023-00222070, grant no. RS-2024-00445081, grant no. RS-2024-00451173), and Samsung Electronics.

References

1. Kum, H. *et al.* Epitaxial growth and layer-transfer techniques for heterogeneous integration of materials for electronic and photonic devices. *Nature Electronics* vol. 2 439–450 Preprint at https://doi.org/10.1038/s41928-019-0314-2 (2019).
2. Kim, H. *et al.* Remote epitaxy. *Nature Reviews Methods Primers* **2**, (2022).
3. Chang, C. S. *et al.* Remote epitaxial interaction through graphene. *Science Advances 9.42* (2023).
4. Kim, J. *et al.* Principle of direct van der Waals epitaxy of single-crystalline films on epitaxial graphene. *Nat Commun* **5**, (2014).
5. Narayan, J. Recent progress in thin film epitaxy across the misfit scale (2011 Acta Gold Medal Paper). *Acta Mater* **61**, 2703–2724 (2013).
6. Kum, H. S. *et al.* Heterogeneous integration of single-crystalline complex-oxide membranes. *Nature* **578**, 75–81 (2020).
7. Kim, Y. *et al.* Remote epitaxy through graphene enables two-dimensional material-based layer transfer. *Nature* **544**, 340–343 (2017).
8. Qiao, K. *et al.* Graphene Buffer Layer on SiC as a Release Layer for High-Quality Freestanding Semiconductor Membranes. *Nano Lett* **21**, 4013–4020 (2021).
9. Emtsev, K. V. *et al.* Towards wafer-size graphene layers by atmospheric pressure graphitization of silicon carbide. *Nat Mater* **8**, 203–207 (2009).
10. Berger, C. *et al.* Electronic Confinement and Coherence in Patterned Epitaxial Graphene. *Science (1979)* **312**, 1191–1196 (2006).
11. Juang, Z. Y. *et al.* Synthesis of graphene on silicon carbide substrates at low temperature. *Carbon N Y* **47**, 2026–2031 (2009).
12. Yuan, W., Li, C., Li, D., Yang, J. & Zeng, X. Preparation of single- and few-layer graphene sheets using Co deposition on sic substrate. *J Nanomater* **2011**, (2011).

13. Iacopi, F. *et al.* A catalytic alloy approach for graphene on epitaxial SiC on silicon wafers. *J Mater Res* **30**, 609–616 (2015).

14. Røst, H. I. *et al.* Low-Temperature Growth of Graphene on a Semiconductor. *Journal of Physical Chemistry C* **125**, 4243–4252 (2021).

15. Escobedo-Cousin, E. *et al.* Local solid phase epitaxy of few-layer graphene on silicon carbide. in *Materials Science Forum* vols 717–720 629–632 (Trans Tech Publications Ltd, 2012).

16. MacHáč, P., Fidler, T., Cichoň, S. & Mišková, L. Synthesis of graphene on SiC substrate via Ni-silicidation reactions. *Thin Solid Films* **520**, 5215–5218 (2012).

17. Macháč, P., Fidler, T., Cichoň, S. & Jurka, V. Synthesis of graphene on Co/SiC structure. *Journal of Materials Science: Materials in Electronics* **24**, 3793–3799 (2013).

18. Escobedo-Cousin, E. *et al.* Solid phase growth of graphene on silicon carbide by nickel silicidation: Graphene formation mechanisms. in *Materials Science Forum* vols 778–780 1162–1165 (Trans Tech Publications Ltd, 2014).

19. Lim, S. *et al.* Interfacial reactions in Ni/6H-SiC at low temperatures. *J Nanosci Nanotechnol* **16**, 10853–10857 (2016).

20. Kwon, Y., An, B. S. & Yang, C. W. Direct observation of interfacial reaction of Ni/6H-SiC and carbon redistribution by in situ transmission electron microscopy. *Mater Charact* **140**, 259–264 (2018).

21. Hähnel, A., Ischenko, V. & Woltersdorf, J. Oriented growth of silicide and carbon in SiC-based sandwich structures with nickel. *Mater Chem Phys* **110**, 303–310 (2008).

22. Chou, T. C., Joshi, A. & Wadsworth, J. Solid state reactions of SiC with Co, Ni, and Pt. *J Mater Res* **6**, 796–809 (1991).

23. Tang, W. M., Zheng, Z. X., Ding, H. F. & Jin, Z. H. *A Study of the Solid State Reaction between Silicon Carbide and Iron*. *Materials Chemistry and Physics* vol. 74 (2002).

24. Wu, M., Huang, H., Wu, Y. & Wu, X. Mechanism of solid-state diffusion reaction in vacuum between metal (Fe, Ni, and Co) and 4H–SiC. *Ceram Int* **50**, 17930–17939 (2024).

25. Schlesinger, M. E. *Thermodynamics of Solid Transition-Metal Silicides*. *Chem. Rev* vol. 90 https://pubs.acs.org/sharingguidelines (1990).

26. Nash, B. P. & Nash, A. *The Ni-Si (Nickel-Silicon) System Equilibrium Diagram*.

27. Perring, L., Bussy, F., Gachon, J. C. & Feschotte, P. *The Ruthenium-Silicon System*. *Journal of Alloys and Compounds* vol. 284 (1999).

28. Mattevi, C., Kim, H. & Chhowalla, M. A review of chemical vapour deposition of graphene on copper. *J Mater Chem* **21**, 3324–3334 (2011).

29. Cao, Y., Nyborg, L. & Jelvestam, U. XPS calibration study of thin-film nickel silicides. *Surface and Interface Analysis* **41**, 471–483 (2009).

30. Ohtsu, N., Oku, M., Satoh, K. & Wagatsuma, K. Dependence of core-level XPS spectra on iron silicide phase. *Appl Surf Sci* **264**, 219–224 (2013).

31. van Vliet, S., Troglia, A., Olsson, E. & Bliem, R. Identifying silicides via plasmon loss satellites in photoemission of the Ru-Si system. *Appl Surf Sci* **608**, (2023).

32. Hoshino, Y., Matsumoto, S., Nakada, T. & Kido, Y. Interfacial reactions between ultra-thin Ni-layer and clean 6H-SiC(0 0 0 1) surface. *Surf Sci* **556**, 78–86 (2004).

33. Hao, Y. *et al.* Probing layer number and stacking order of few-layer graphene by Raman Spectroscopy. *Small* **6**, 195–200 (2010).

34. Lee, D. S. *et al.* Raman spectra of epitaxial graphene on SiC and of epitaxial graphene transferred to SiO2. *Nano Lett* **8**, 4320–4325 (2008).

35. Bae, S. H. *et al.* Graphene-assisted spontaneous relaxation towards dislocation-free heteroepitaxy. *Nat Nanotechnol* **15**, 272–276 (2020).

36. Wang, Y. *et al.* Flexible graphene-assisted van der Waals epitaxy growth of crack-free AlN epilayer on SiC by lattice engineering. *Appl Surf Sci* **520**, (2020).

37. Pradhan, D. K. *et al.* Materials for high-temperature digital electronics. *Nat Rev Mater* (2024) doi:10.1038/s41578-024-00731-9.

38. Zhou, C. *et al.* Review—The Current and Emerging Applications of the III-Nitrides. *ECS Journal of Solid State Science and Technology* **6**, Q149–Q156 (2017).

39. Gong, J. *et al.* Synthesis and Characteristics of Transferrable Single-Crystalline AlN Nanomembranes. *Adv Electron Mater* **9**, (2023).

40. Xu, Y. *et al.* Growth Model of van der Waals Epitaxy of Films: A Case of AlN Films on Multilayer Graphene/SiC. *ACS Appl Mater Interfaces* **9**, 44001–44009 (2017).

41. Yu, Y. *et al.* Demonstration of epitaxial growth of strain-relaxed GaN films on graphene/SiC substrates for long wavelength light-emitting diodes. *Light Sci Appl* **10**, (2021).

42. Avouris, P. & Dimitrakopoulos, C. *Graphene: Synthesis and Applications*. (2012).

43. Chen, W. & Capano, M. A. Growth and characterization of 4H-SiC epilayers on substrates with different off-cut angles. *J Appl Phys* **98**, (2005).

44. Chen, Z. *et al.* Improved Epitaxy of AlN Film for Deep-Ultraviolet Light-Emitting Diodes Enabled by Graphene. *Advanced Materials* **31**, (2019).

45. Kresse, G. & Furthmü, J. Efficient iterative schemes for ab initio total-energy calculations using a plane-wave basis set. *Phys Rev B* **54**, 11169–186 (1996).

46. Blochl, P. E. Projector augmented-+rave method. *Phys Rev B* **50**, 17953–17979 (1994).

47. Perdew, J. P., Burke, K. & Ernzerhof, M. Generalized Gradient Approximation Made Simple. *Phys Rev Lett* **77**, 3865–3868 (1996).

48. Makov, G. & Payne, M. C. Periodic boundary conditions in ab intio calculations. *Phys Rev B* **51**, 4014–4022 (1995).

49. Nosé, S. A unified formulation of the constant temperature molecular dynamics methods. *J Chem Phys* **81**, 511–519 (1984).

50. Hoover, W. G. Canonical dynamics: Equilibrium phase-space distributions. *Phys Rev A (Coll Park)* **31**, (1985).

Figures

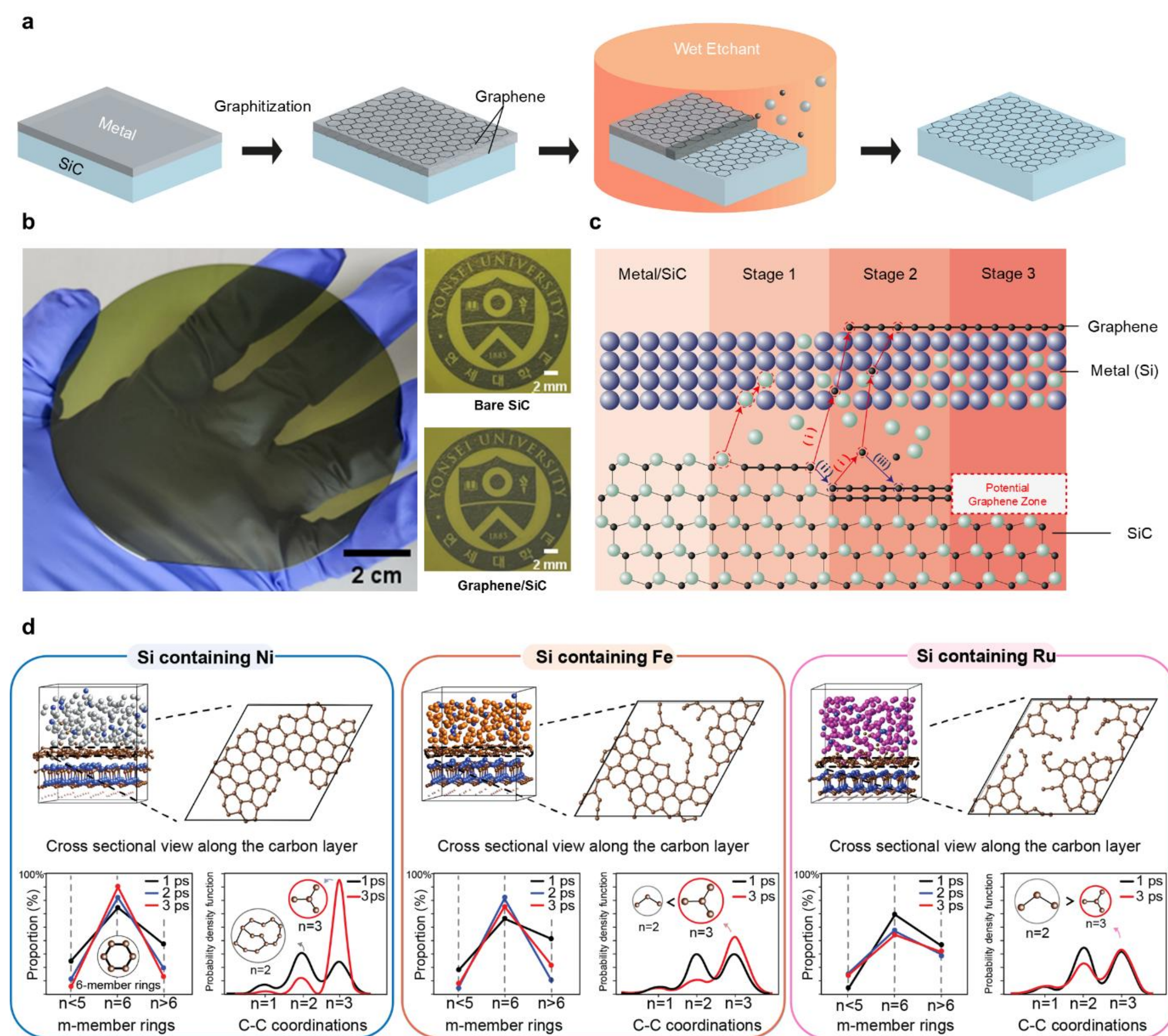

Figure 1 | The MAG process and DFT model. a, Schematic representation of the MAG process. **b,** Photograph of graphene on a 4-inch wafer SiC (left), with zoomed-in images showing bare SiC (upper right) and 4 ML graphene on MAG-treated SiC (lower right). The darker appearance of the graphene sample indicates reduced visible light transmittance. **c,** Schematic illustration of the carbon distribution model during the solid-state reaction in the MAG process. **d,** Structural evolution of a carbon layer at the metal-SiC interface during AIMD simulations. The overall 3D view and top view emphasize the differences in the trajectories of carbon atoms at the interface depending on the metal elements. The computed changes in the m-membered rings centered on carbon atoms and coordination numbers clearly reveal that only Ni metal stabilizes a graphene-like structure at the interface, while this stabilization effect is not evident for Fe and Ru metals.

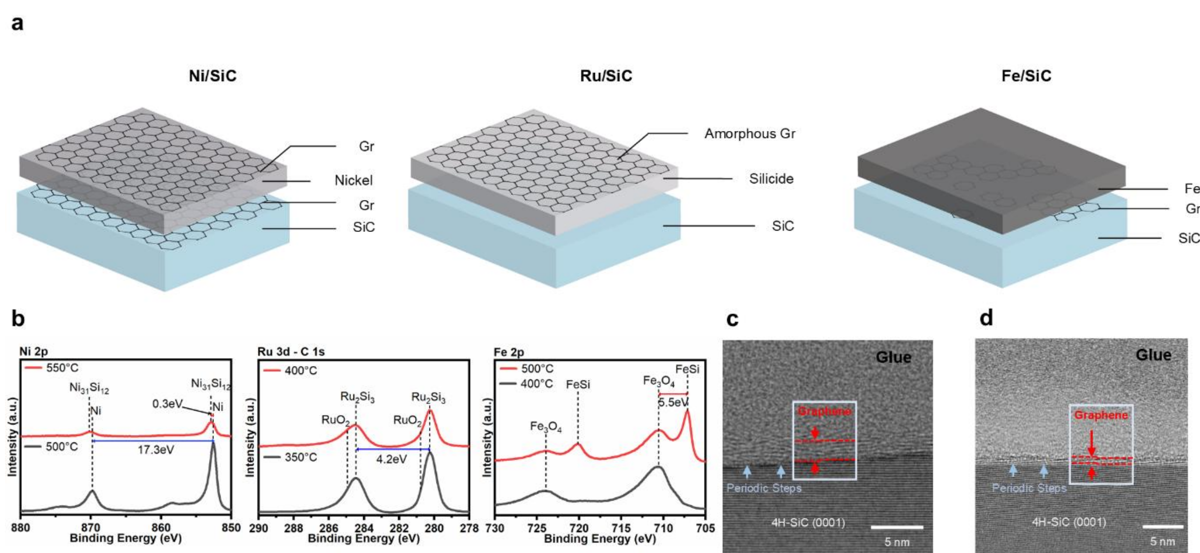

Figure 2 | Metal effect in the MAG process, and experimental investigations. a, Schematic representation of the metal effect in the MAG process, as calculated by DFT calculation and experimental results. The entire interface graphene layer was detected only when using Ni as a catalyst. **b,** X-ray spectra showing Ni 2p (left), Ru 3d (center), and Fe 2p (right). **c,** HR-TEM cross-sectional image of MAG-treated SiC, annealed at 500°C after depositing a 50 nm Ni layer. **d,** HR-TEM cross-sectional image of MAG-treated SiC, annealed at 500°C after depositing an 8 nm Ni layer. The graphene thickness was reduced to 1 layer by lowering the initial metal thickness.

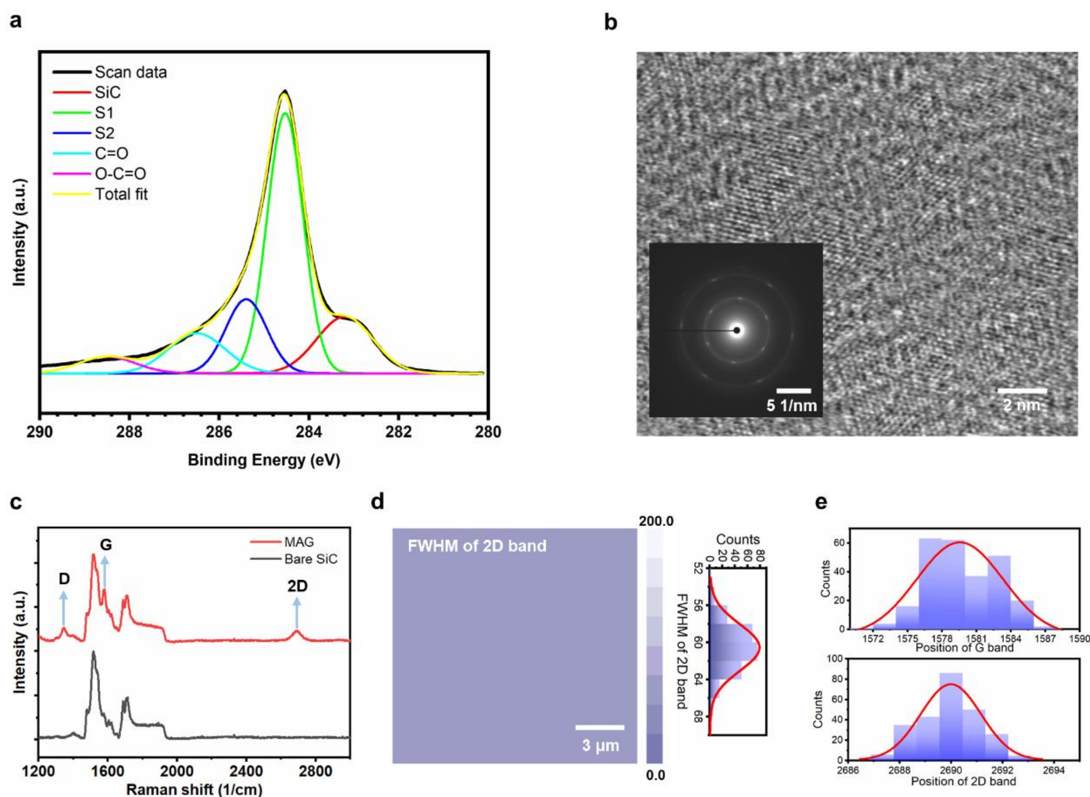

Figure 3 | Wafer-scale single-crystalline graphene formed on SiC via the MAG process. a, XPS spectra of the C 1s region, showing graphene on the entire SiC. **b,** Plan-view TEM image with SAED patterns of graphene transferred onto SiO_2, verifying the single-crystalline nature of the graphene. **c,** Raman spectra showing distinct D, G, and 2D peaks, indicating the presence of graphene on SiC. **d,** Raman map of the FWHM of the 2D peak, demonstrating the uniformity of graphene thickness. A total of 256 points were measured within a 15 μm × 15 μm Raman mapping area. **e,** Histogram of the G and 2D peak positions, indicating overall uniform graphene quality, and thickness.

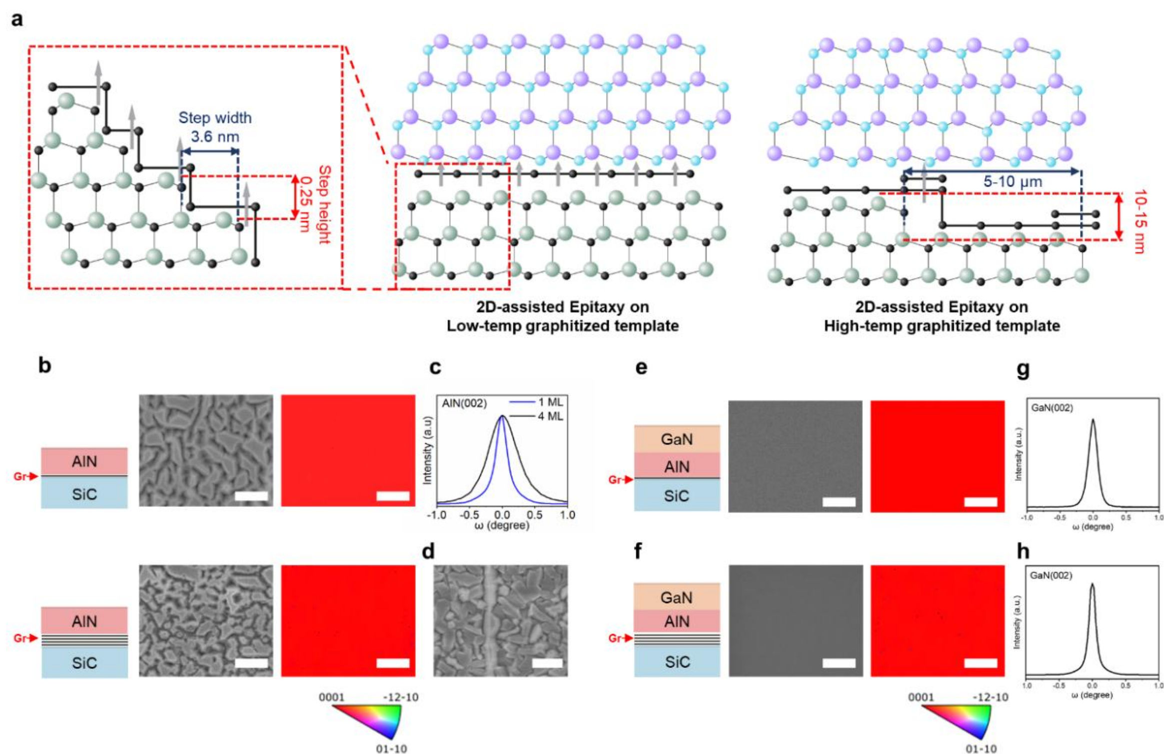

Figure 4 | Free-standing III-nitride membranes synthesized on MAG-treated graphene/SiC templates. a, Schematic illustration of 2D-assisted epitaxy on MAG-treated graphitized SiC and high-temperature graphitized SiC. Unlike high-temperature graphitization, MAG-treated SiC avoids step bunching, offering potential advantages for growing high-quality membranes through 2D-assisted epitaxy. **b,** Schematic illustration of the grown film structure (left), SEM image (center), and EBSD map (right), showing the highly single-crystalline nature of the AlN membrane over a large scale on 1 ML Gr/SiC and 4 ML Gr/SiC templates, respectively. **c,** XRD ω-scan of both templates. The FWHM of the AlN (002) peak increases with graphene layer thickness. **d,** SEM image of AlN grown on high-temperature graphitized SiC, showing a preference for nucleation on step edges and a polycrystalline nature on terraces. **e,** Schematic illustration of the grown film structure (left), SEM image (center), and EBSD map (right), showing the highly single-crystalline nature of the GaN membrane over a large scale on the AlN/1 ML Gr/SiC template. **f,** Schematic illustration of the grown film structure (left), SEM image (center) and EBSD map (right), showing the highly single-crystalline nature of the GaN membrane over a large scale on the AlN/4 ML Gr/SiC template. **g-h,** XRD ω-scans of GaN membranes grown on AlN/1 ML Gr/SiC and AlN/4 ML Gr/SiC templates, respectively, showing no significant differences. The scale bars in all SEM images and EBSD map are 300 nm.

SUPPLEMENTARY INFORMATION

Low-temperature wafer-scale graphitization of silicon-carbide substrates towards reusable ultra-wide bandgap substrates

Se H. Kim, Hanjoo Lee, Dong Gwan Kim, Donghan Kim, Seugki Kim, Hyunho Yang, Yunsu Jang, Jangho Yoon, Hyunsoo Kim, Seoyong Ha, ByoungTak Lee, Jung-Hee Lee, Roy Byung Kyu Chung, Hongsik Park, Sungkyu Kim, Tae Hoon Lee, Hyun S. Kum

Supplementary Note 1 | DFT Simulation modeling workflow

The slab models had dangling bonds on the vacuum surface, which were terminated with pseudo-hydrogen atoms with appropriate fractional charges to prevent the generation of surface states. To determine the vacuum level, dipole corrections were introduced to compensate for the artificial dipole moment at the open ends (20 Å vacuum space along the c-axis) arising from the periodical boundary condition imposed in these calculations.

To search for an ideal hetero-interface, combinations of substrate and film Miller indices were scanned[1]. From these scans, optimized domain-matched configurations with the lowest mismatch strain, supercell area, and lattice vector length were identified. This process resulted in the discovery of domain-matched heterostructures between SiC and graphene surfaces, with a lattice mismatch of less than 4%, as shown in Supplementary Fig. 3c. A similar matching procedure was applied to generate the interface between the SiC/graphene and metal layers.

To replicate the graphene-formaton phenomenon during the MAG (Metal-Assisted Graphitization) process, AIMD simulations were performed in three main steps: (i) a Si-containing metal layer was generated by substituting (at. 20%) Si atoms for Ni; (ii) the SiC/Graphene/Si-dissolved metal heterostructure was relaxed through energy minimization to stabilize the initial atomic configuration of each model; and (iii) random displacements were introduced to the carbon atoms in the graphene layer to study the stabilization effect of metal catalysts from the interface interaction beetween the metal and graphene layers[2–4].

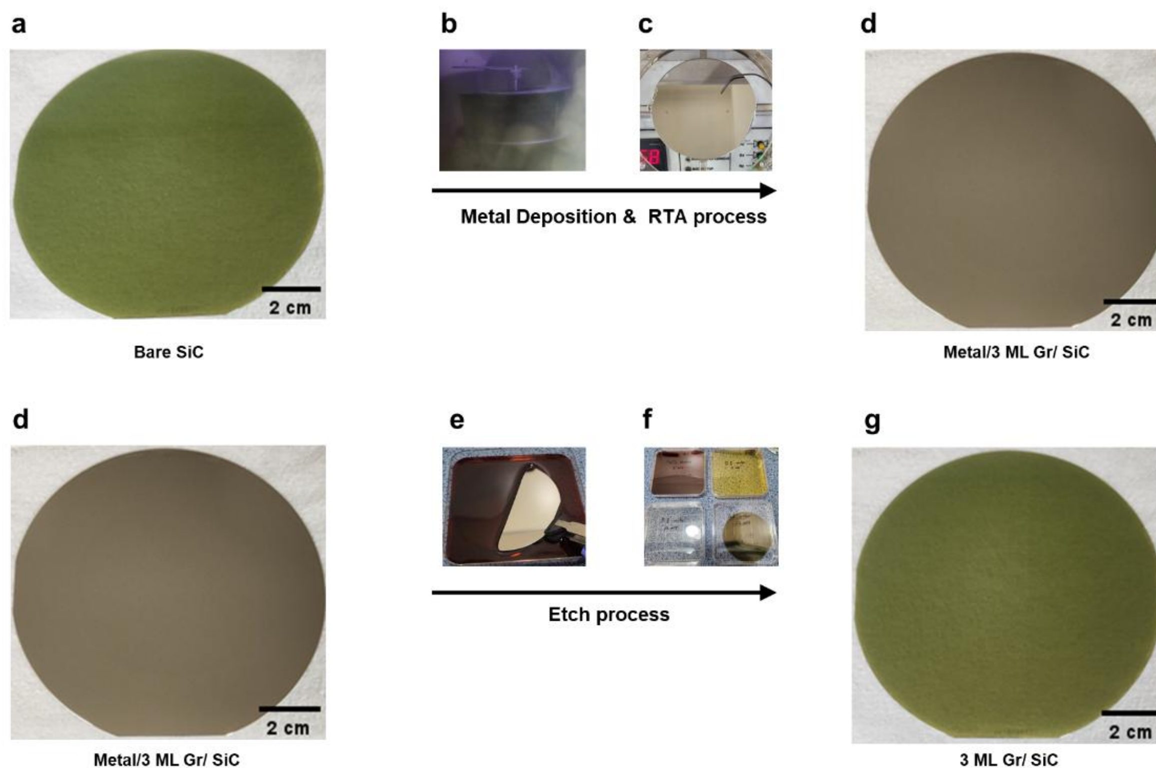

Supplementary Fig. 1 | Detailed MAG process. a, The SiC wafer is cleaned sequentially in acetone (5 minutes), and isopropyl alcohol (IPA) for 5 minutes each using an ultrasound bath and then dried with a nitrogen gun. **b,** Ni is deposited onto the SiC by sputtering at a pressure of 5×10^{-4} Torr in an Ar ambient (50 sccm) for 20 minutes. **c,** The sample is annealed in a rapid thermal annealing (RTA) chamber under specific conditions: a heating speed of 12°C/s, annealing for 3 minutes, and cooling by turning off the power. **d,** Graphene forms at the Ni/SiC interface through the MAG process. **e,** Ni is etched away using ferric chloride ($FeCl_3$) to expose the interface graphene. **f,** Once all visible traces of Ni are removed, the sample is gently agitated in fresh $FeCl_3$, followed by rinsing in deionized water. The surface is kept wet to prevent redeposition of Ni residues. **g,** The final result of the MAG process demonstrates graphene formation on the entire 4-inch SiC substrate.

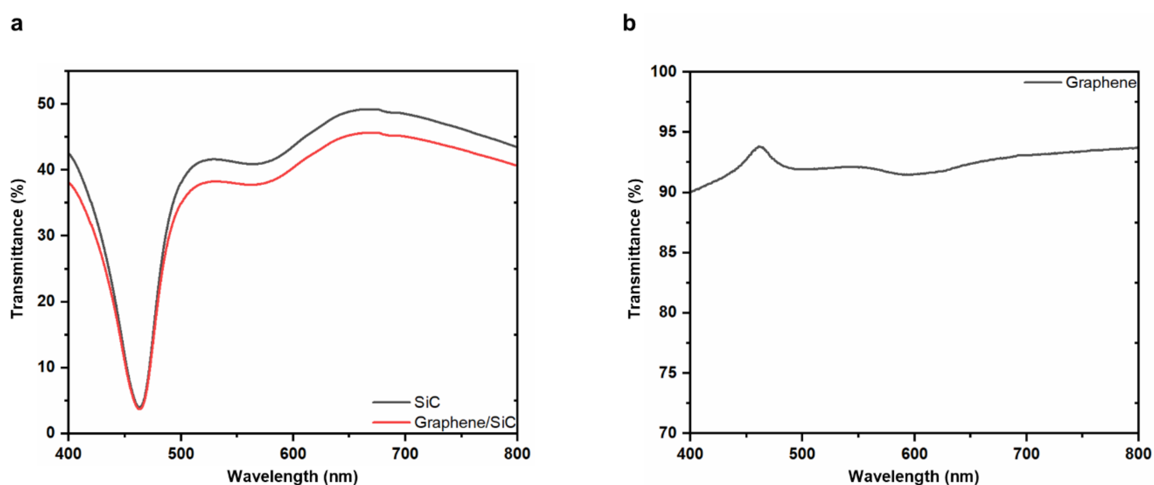

Supplementary Fig. 2 | UV-vis transmittance spectra in the wavelength range of 400 nm - 800 nm. a, UV-vis transmittance spectra of a SiC without graphene (red) and with graphene (black), showing reduced transmittance due to the graphene layer. **b,** The transmittance of graphene in the visible light is measured at 92.1% at 550 nm, indicating the presence of approximately 3.4 graphene monolayers on the SiC.

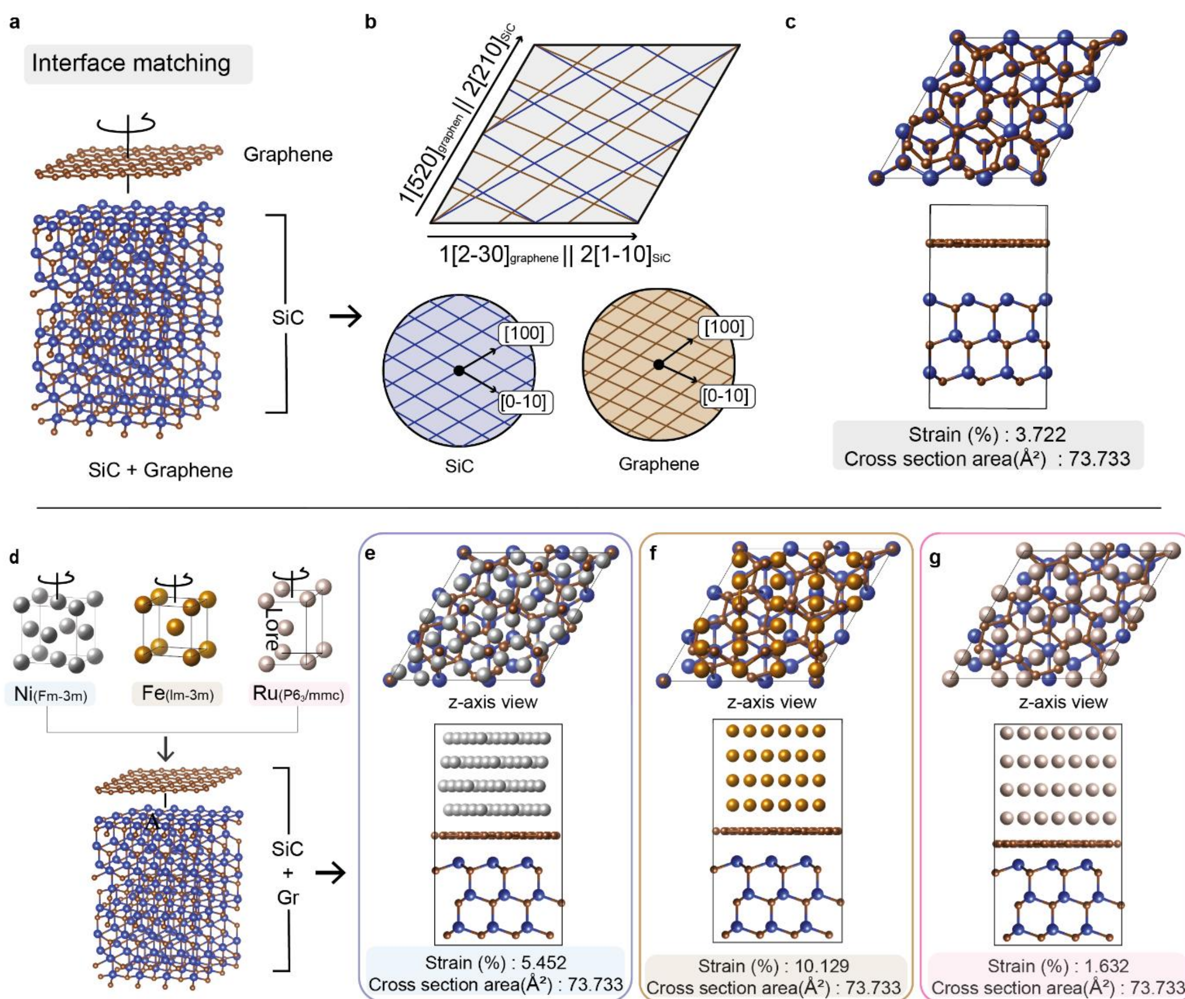

Supplementary Fig. 3 | Interface matching for modeling the SiC/graphene/metal structures. a, Interface construction for the SiC/Graphene structure. **b,** Domain-matched supercell construction for the SiC (blue) and graphene (brown) layers with corresponding lattice unit vectors. **c,** Top and side views of the optimized interface configuration (Si atoms are colored in blue, and C atoms are dark brown). **d,** Schematic illustration of the interface-matching process for the SiC/Graphene/Metal system, along with the crystal structures of Ni (Fm-3m), Fe (Im-3m), and Ru ($P6_3$/mmc) used for interface matching. **e-g,** Matched heterostructures used for the AIMD simulations: Ni (5.452% strain), Fe (10.129% strain), and Ru (1.632% strain), each with a cross-sectional area of 43.256 $Å^2$.

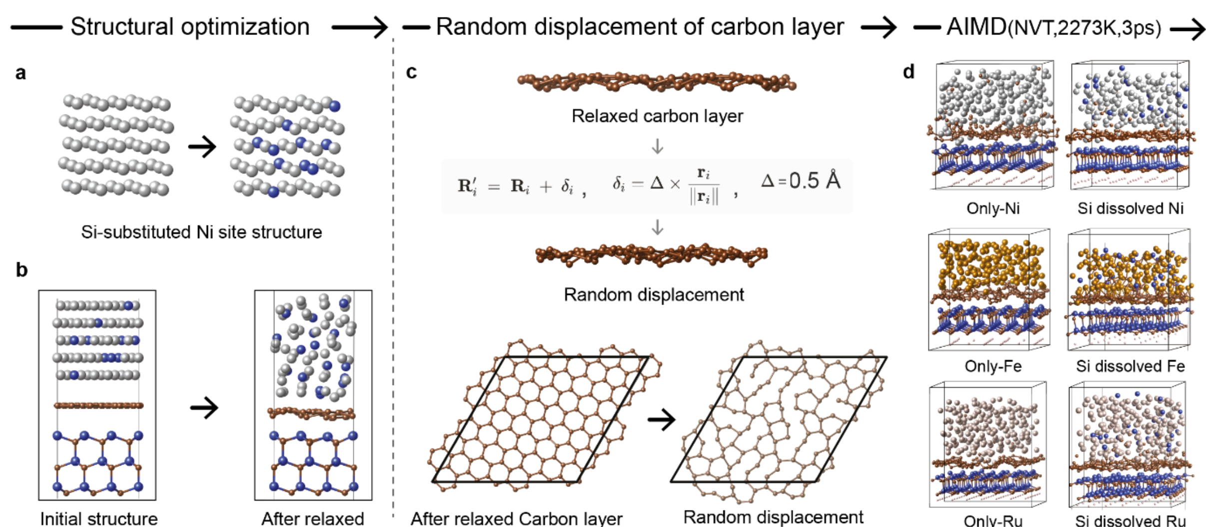

Supplementary Fig. 4 | Modeling workflow and AIMD simulations for the SiC/graphene/metal heterostructures. a, Formation of Si-containing metal layers. **b,** An example of a relaxed configuration of the SiC/Graphene/Metal model after energy minimization. **c,** Generation of randomly-displaced carbon atoms in the graphene layer to study the stabilization effect of metal catalysts. **d,** Model configurations used in this study. Both pure and Si-containing metal layers were investigated for each metal using AIMD simulations.

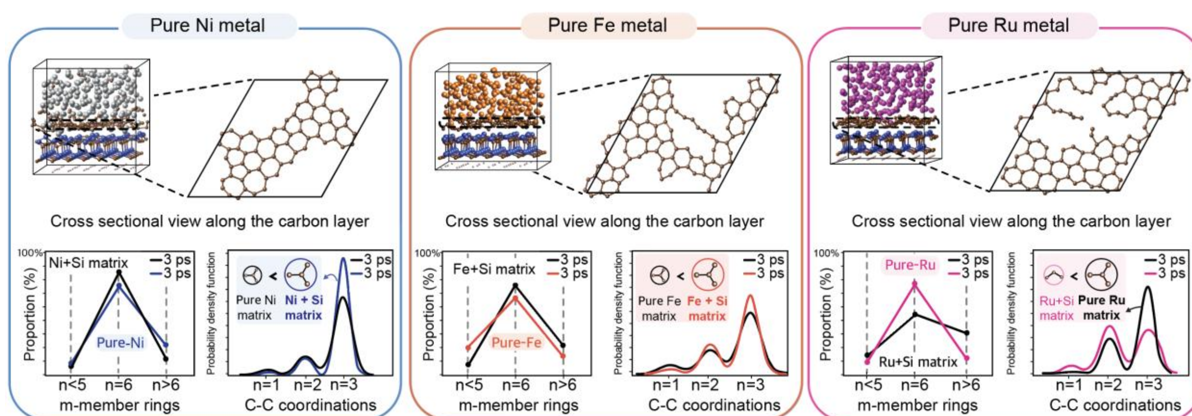

Supplementary Fig. 5 | AIMD simulations with metal layers without Si alloying. For pure Ni and Fe models, the number of six-fold rings and three-fold-coordinated carbon atoms was consistently lower than in their Si-dissolved counterpart, underscoring the critical role of dissolved silicon in enhancing the structural transition toward graphene-like configurations. In contrast, graphene formation in the Ru matrix occurs only when silicon is not dissolved in the Ru bulk. Among the models studied, only the Si-dissolved Ni model provided an environment where carbon atoms could readily reorganize, enabling the formation of stable, two-dimensional graphene configurations.

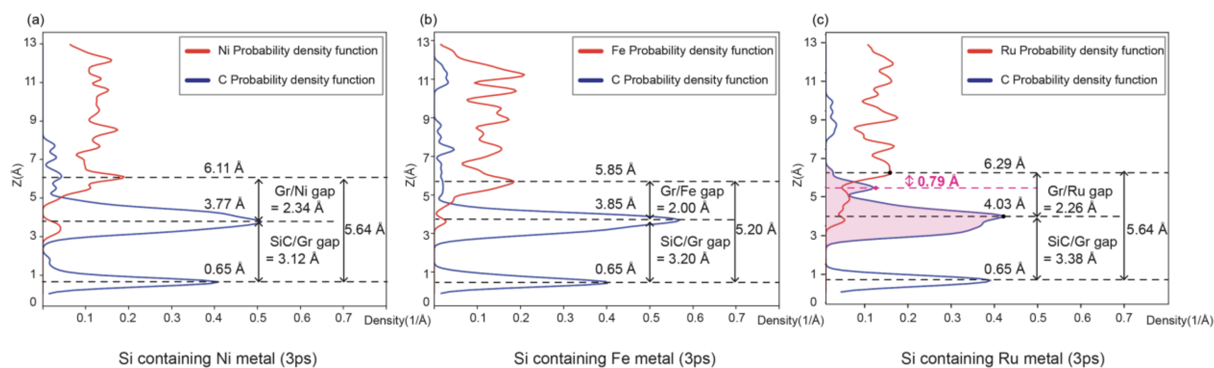

Supplementary Fig. 6 | Study on the van der Waals gap between the metal and carbon layers using the probability-density function. The width of the van der Waals gap observed in (a) the Si-dissolved Ni model, (b) the Si-dissolved Fe model, and (c) the Si-dissolved Ru model. The Ni-containing model maintained a consistent van der Waals gap between the metal and the topmost carbon layer, whereas the Fe- and Ru-containing models exhibited a collapse of the gap.

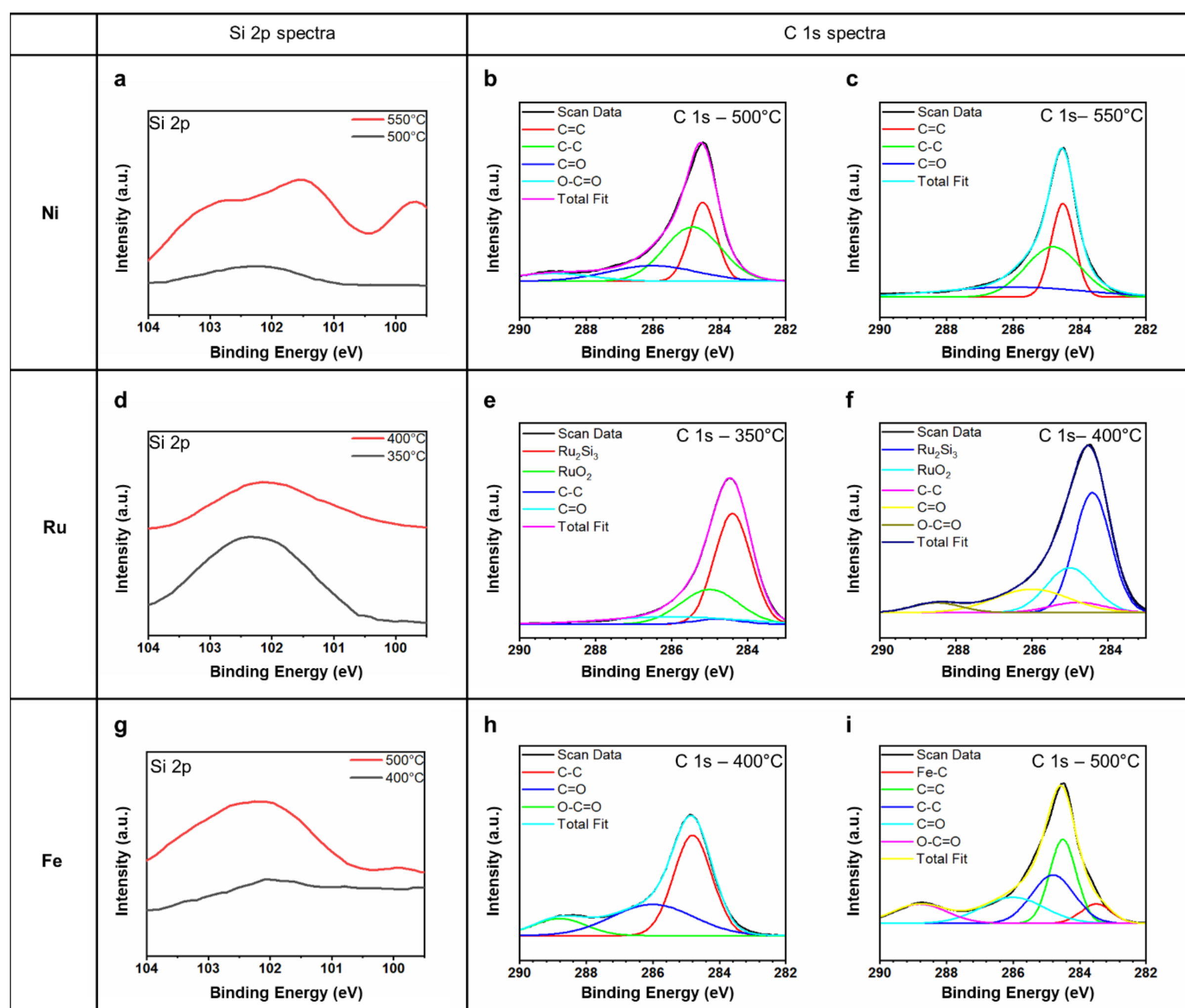

Supplementary Fig. 7 | X-ray photoelectron spectra of metal/SiC after annealing at various temperatures. a, Comparison of the Si 2p spectra in Ni/SiC for each annealing temperature. **b**, C 1s spectra of Ni/SiC annealing at 500ºC. **c,** C 1s spectra of Ni/SiC annealing at 550ºC. **d,** Comparison of the Si 2p spectra in Ru/SiC for each annealing temperature. **e**, C 1s spectra of Ru/SiC annealing at 350ºC. **f,** C 1s spectra of Ru/SiC annealing at 400ºC. **g,** Comparison of the Si 2p spectra in Fe/SiC for each annealing temperature. **h**, C 1s spectra of Fe/SiC annealing at 400ºC. **i,** C 1s spectra of Fe/SiC annealing at 500ºC. All spectra were calibrated using the C-C bond (284.8eV) and cross-checked with Raman spectra (see Supplementary Fig. 8) and XRD (see Supplementary Fig. 9) results. The thickness of the deposited metal layer exceeded the detection limit depth of XPS (typically around 10nm) indicating that the detected Si and C atoms originated from the SiC.

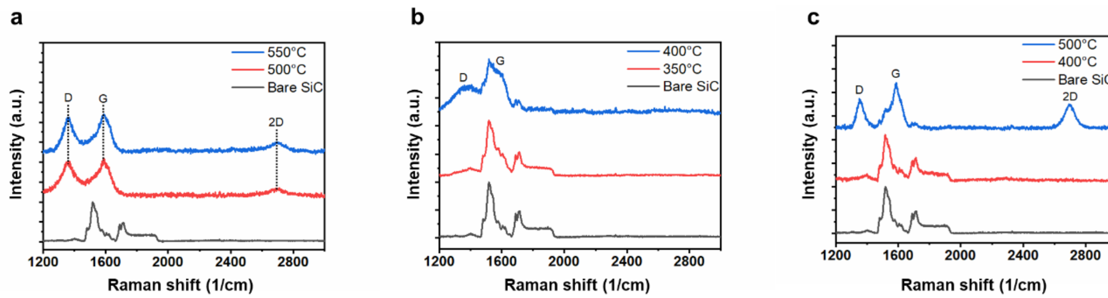

Supplementary Fig. 8 | Raman spectra after annealing at corresponding temperatures. a, Comparison of the Ni/SiC Raman spectra at different annealing temperatures. **b**, Comparison of the Ru/SiC Raman spectra at different annealing temperatures. **c**, Comparison of the Fe/SiC Raman spectra at different annealing temperatures. At 500ºC for Ni, 400ºC for Ru, and 500ºC for Fe, liberated carbon diffused outward and formed graphene on the metal surface, consistent with XPS results.

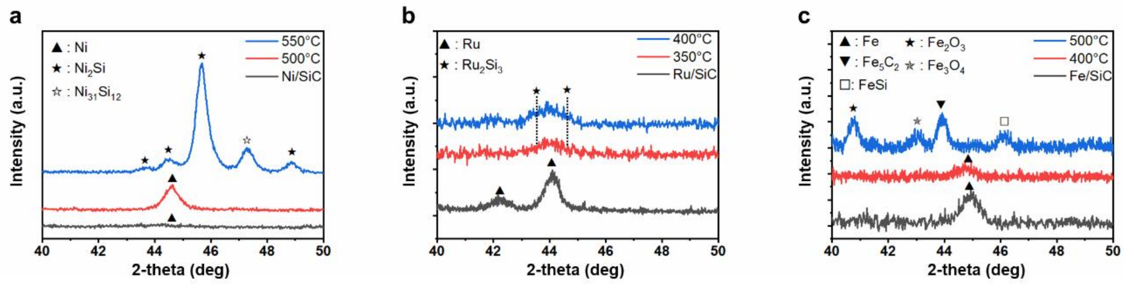

Supplementary Fig. 9 | X-ray diffraction patterns after annealing at corresponding temperatures. a, Comparison of the Ni/SiC X-ray diffraction patterns at various annealing temperatures. The reference patterns correspond to JCPDS no. 71-4655 for Ni, JCPDS no. 79-3559 for Ni_2Si, and JCPDS no. 17-0222 for $Ni_{31}Si_{12}$. **b**, Comparison of the Ru/SiC X-ray diffraction patterns at various annealing temperatures. The reference patterns correspond to JCPDS no. 73-7011 for Ru, and JCPDS no. 88-0895 for Ru_2Si_3. **c**, Comparison of the Fe/SiC X-ray patterns at various annealing temperatures. The reference patterns correspond to JCPDS no. 76-6588 for Fe, JCPDS no. 79-3559 for FeSi, JCPDS no. 89-8103 for Fe2O3, JCPDS no. 71-6336 for Fe_3O_4, and JCPDS no. 89-8968 for Fe_5C_2.

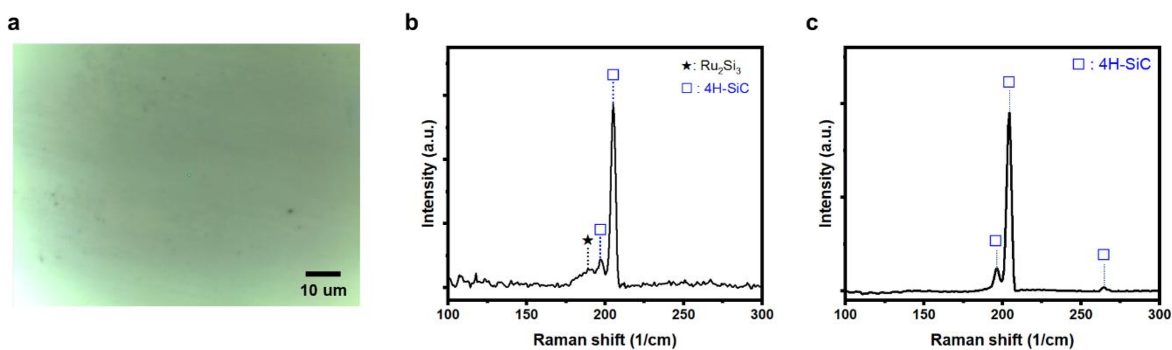

Supplementary Fig. 10 | Optical image and Raman spectra of the Ru/SiC annealed at 350° C. a-b, Raman spectra with optical image reveal the presence of Ru_2Si_3 peak at the 203 cm^{-1}, consistent with XPS and XRD results. **c,** Raman spectra of bare SiC in range of 50 cm^{-1} to 500 cm^{-1}, indicate the absence of the 203 cm^{-1} peak.

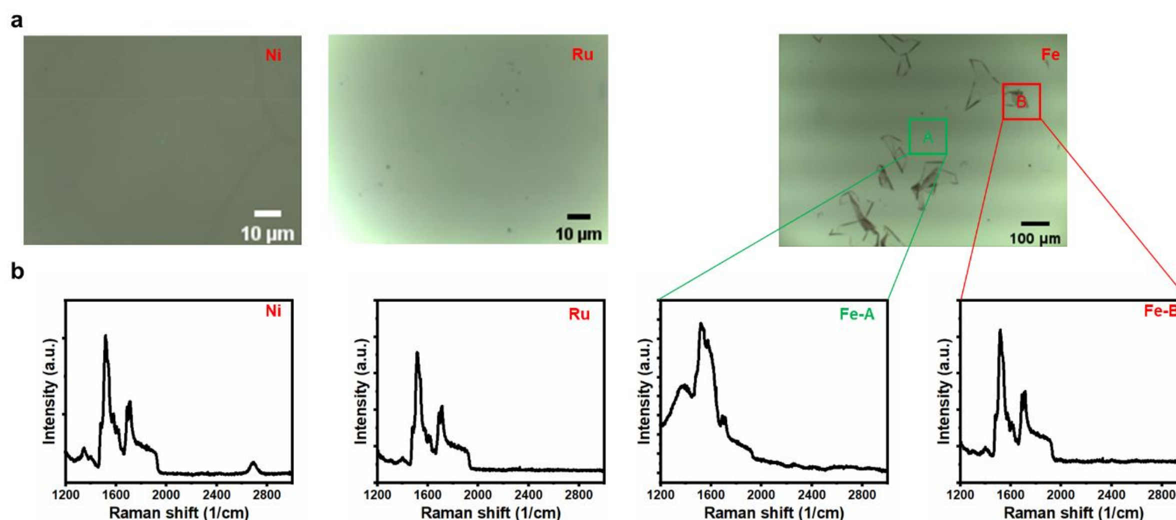

Supplementary Fig. 11 | Micrography and Raman spectra of various metals on SiC after annealing at corresponding temperatures and etching with the appropriate etchant. a, Micrography of Ni/SiC annealed at 500°C and etched with $FeCl_3$, Fe/SiC annealed at 400°C and etched with $FeCl_3$, and Ru/SiC annealed at 350°C and etched with NaOCl. **b,** Raman spectra of each result, showing that only Ni enables the graphene formation on SiC.

a

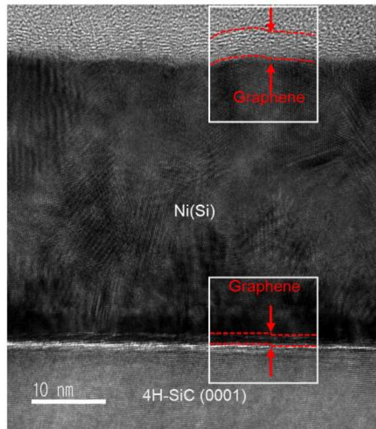

b

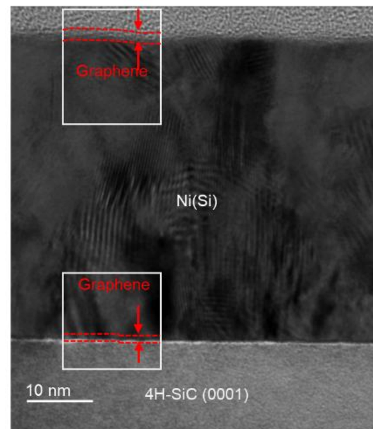

Supplementary Fig. 12 | TEM images of Ni/SiC structure annealed at 500°C and 320°C respectively, measured at 10 nm scale. a, TEM images of Ni/SiC annealed at 500°C. **b,** TEM images of Ni/SiC annealed at 320°C. The TEM images show the graphene layer not only on the metal surface, but also at the Ni/SiC interface. The thickness of graphene is slightly bigger when increasing the annealing temperature, indicating the MAG process is a temperature-driven.

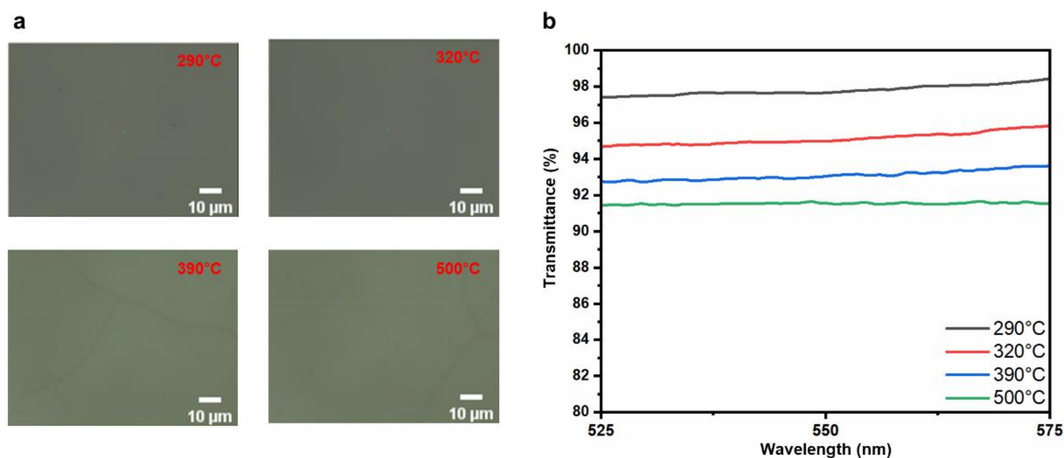

Supplementary Fig. 13 | Optical images and UV-visible spectra after annealing at the corresponding temperatures and etching with $FeCl_3$. a, Optical images after annealing at corresponding temperatures and etching, confirming the absence of residuals and the formation of a macroscopic graphene film. **b,** UV-visible spectra showing that the MAG process is driven by temperature.

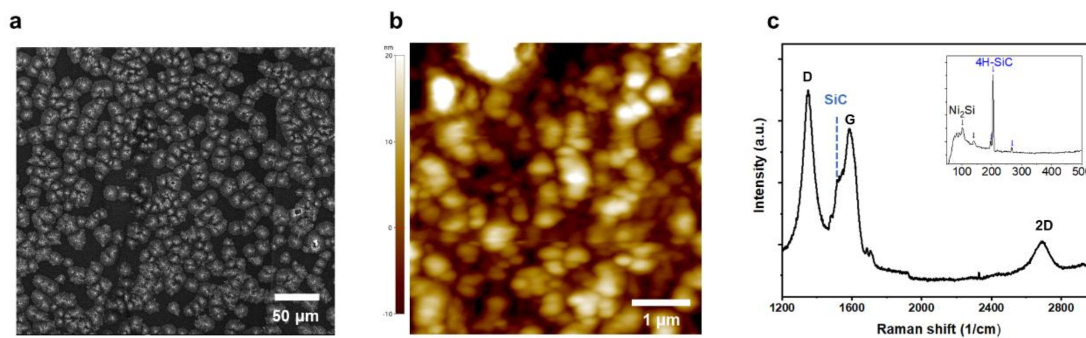

Supplementary Fig. 14 | SEM, AFM images, and Raman spectra after annealing above the silicide formation temperature, and etching the Ni layer with $FeCl_3$. a-b, SEM, and AFM images reveal inhomogeneous reactions, confirming the formation of a non-uniform clustered film. **c,** Raman spectra indicate that the clustered films comprise graphene on a silicide layer.

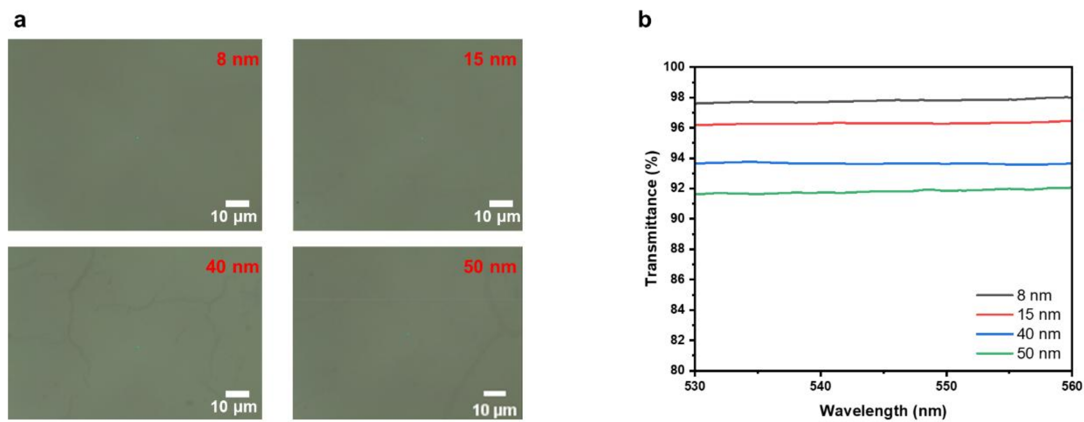

Supplementary Fig. 15 | Optical images and UV-visible spectra for various metal thickness used in MAG process. a, Optical images of samples with different metal thicknesses. **b,** UV-visible spectra indicating that graphene thickness decreases with reduced metal thickness.

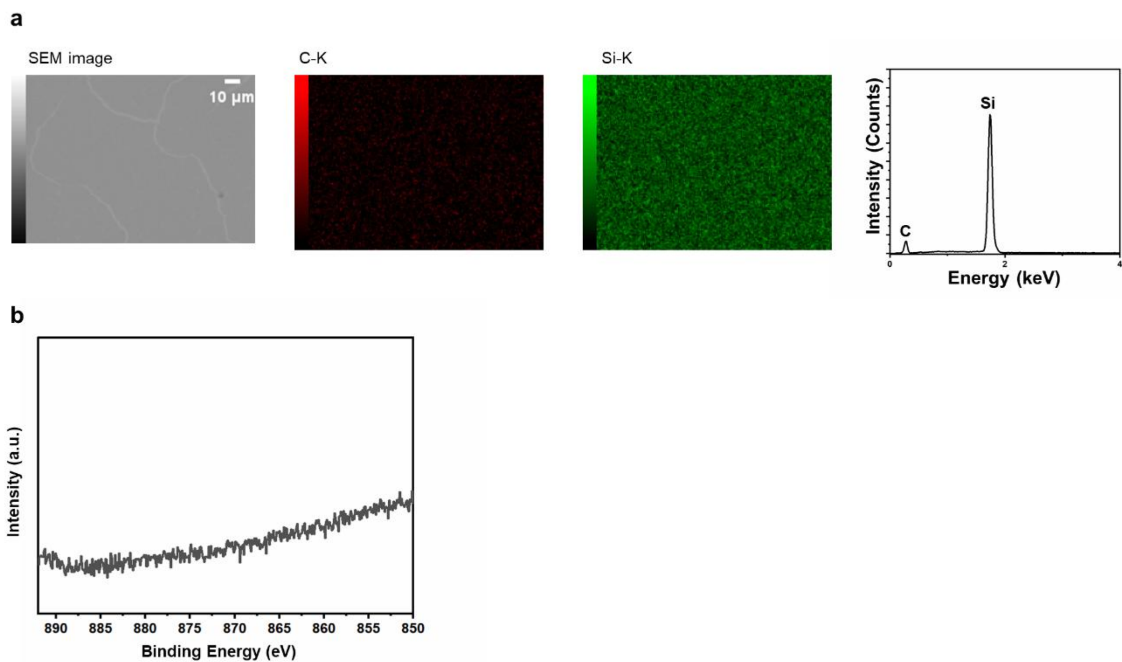

Supplementary Fig. 16 | Energy-dispersive X-ray (EDS) spectra and Ni 2p XPS after etching the unreacted Ni layer with $FeCl_3$. a, EDS scan shows no Ni atoms remaining on the surface. **b,** XPS Ni 2p spectra confirm the absence of detectable Ni. All results indicate the complete removal of Ni.

a

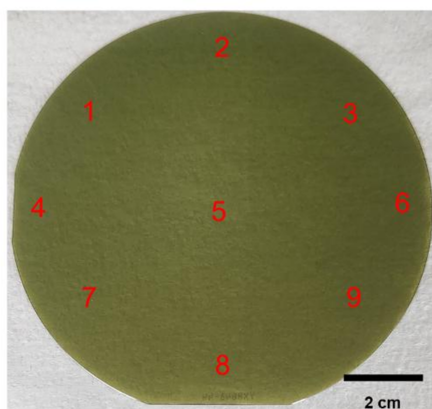

b

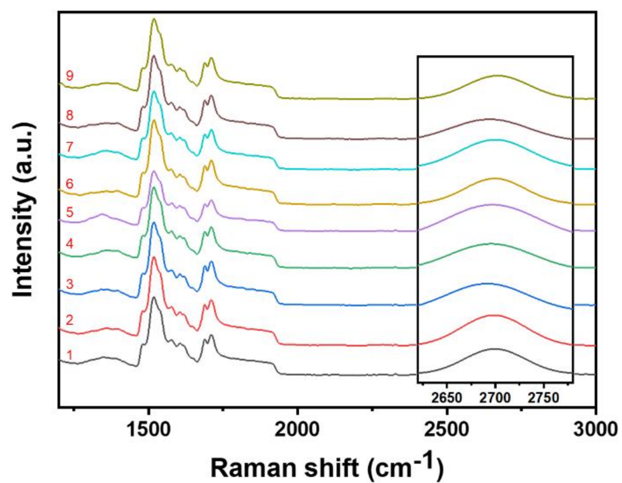

Supplementary Fig. 17 | Raman spectra of a graphitized 4-inch wafer. The wafer was divided into nine areas, and Raman spectra from all regions consistently show the characteristics D, G, and 2D peaks of graphene.

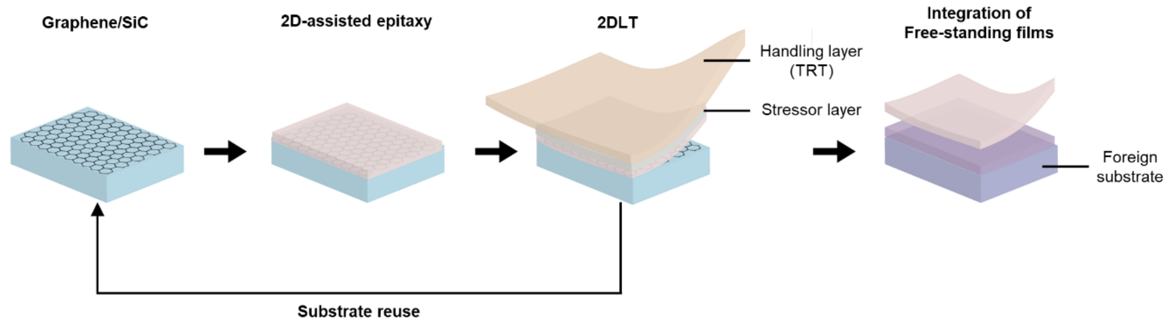

Supplementary Fig. 18 | Schematic illustration of 2D-assisted epitaxy process. The process begins with the graphitization of the SiC to synthesize graphene. This graphitized template is then prepared for 2D-assisted epitaxy, where a wide-bandgap material is grown using a growth chamber, such as MOCVD or MBE, under optimized conditions. After the growth, a stressor layer, typically Ni, is deposited via a sputtering or E-beam evaporator. The thickness and deposition conditions of the Ni layer must be carefully controlled to enable precise exfoliation of the membrane at the van der Waals gap between the membrane and the graphitized SiC interface. Additionally, an adhesion layer may be employed to prevent peeling of the stressor layer. A TRT is then applied as a handling layer, and exfoliation is carried out by smoothly lifting the handling layer. The exfoliated freestanding membrane is subsequently transferred to a foreign substrate. Finally, the TRT is removed by heating the membrane-attached-foreign-sample above 110ºC.

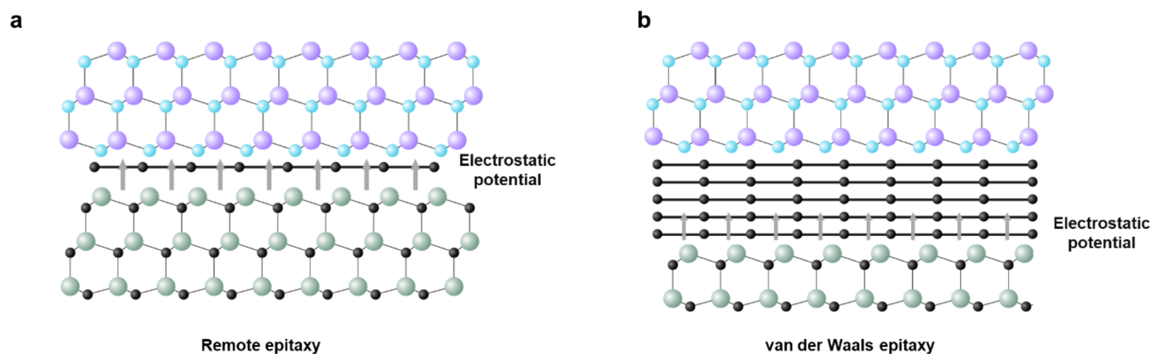

Supplementary Fig. 19 | Schematic illustration of 2D-assisted epitaxy mechanisms. 2D-assisted epitaxy encompasses techniques like remote epitaxy and vdWE, which enable high-quality material growth on 2D materials. However, these techniques differ significantly in their requirements for preparing the graphitized sample. Remote epitaxy requires a minimum graphene layer that is robust enough to withstand the harsh growth environment while allowing the lattice information of the underlying substrate to guide the growth of the crystalline film. In contrast, vdWE does not rely on the lattice information of the substrate. Instead, it demands multi-layers of graphene to completely screen the substrate's electrostatic potential, which enhances the quality of the grown membrane by eliminating substrate interference.

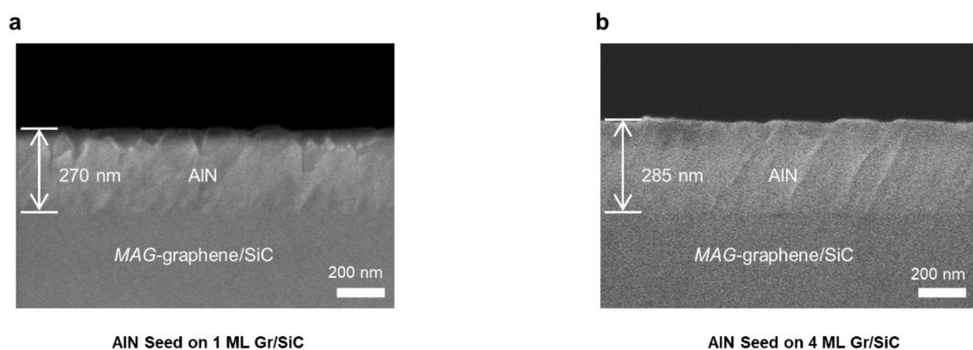

Supplementary Fig. 20 | SEM cross-sectional images of AlN grown on MAG-treated 1 ML graphene and 4 ML graphene on SiC. The thickness of AlN increased from 270 nm to 285 nm, indicating enhanced three-dimensional growth in the vertical direction for the 4 ML graphene sample compared to the 1 ML graphene sample.

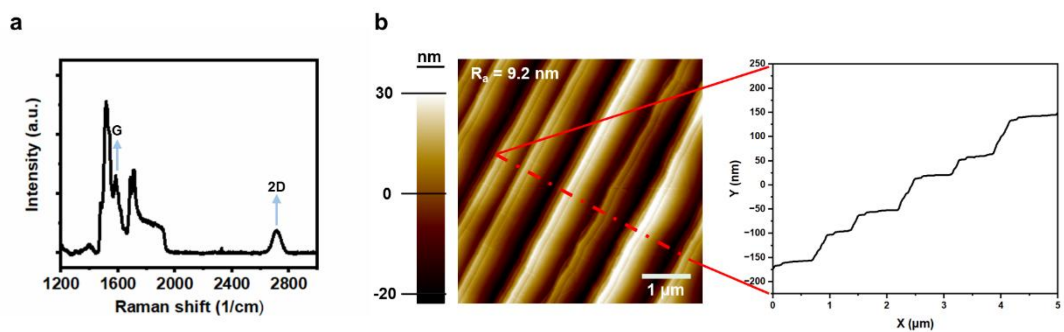

Supplementary Fig. 21 | Raman spectra and AFM images of high-temperature graphitized SiC. a, Raman spectra showing the G and 2D peaks, indicating that graphene covers the entire SiC substrate. **b,** AFM images and line profiles along the red line revealing micrometer-scale terrace widths and nanometer-scale step heights.

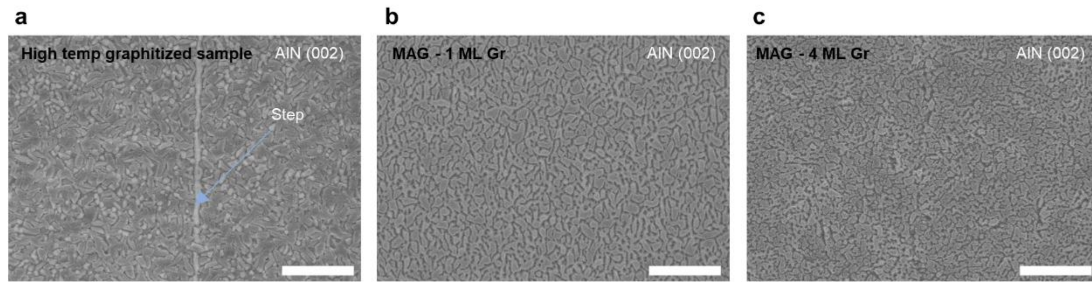

Supplementary Fig. 22 | SEM images of AlN grown on high-temperature graphitized SiC and MAG-graphitized SiC. a, SEM images showing AlN adatoms predominantly nucleating at step edges, with AlN grown on wide terraces exhibiting a poly-crystalline nature. **b-c**, SEM images demonstrating unidirectional growth of AlN crystallites, indicating a single-crystalline nature on both 1 ML Gr/SiC and 4 ML Gr/SiC templates. The scale bar in the SEM images is 300 nm.

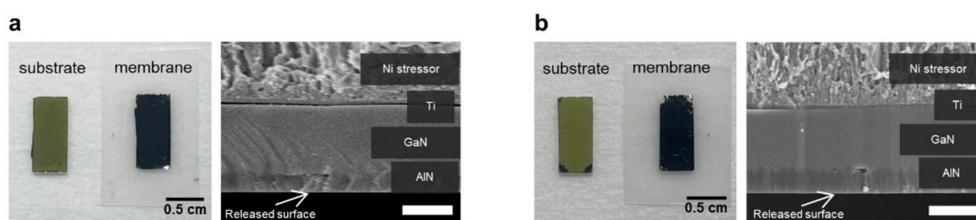

Supplementary Fig. 23 | Camera and SEM images of GaN/AlN grown on MAG-graphitized SiC templates. a, Camera and SEM images of exfoliated GaN/AlN grown on 1 ML Gr/SiC. **b,** Camera and SEM images of exfoliated 4 ML Gr/SiC. Both camera images demonstrate the successful exfoliation of the grown films from the MAG-graphitized SiC templates. The SEM images reveal macroscopically smooth surfaces of the exfoliated films, confirming the effectiveness of the 2DLT process. The scale bar in the SEM images is 500 nm.

Supplementary Table. 1 | Comparison of the crystalline quality of GaN/AlN on MAG-treated SiC with GaN grown on other substrates. The results suggest that our MAG-treated SiC offers a desirable platform for GaN materials. LT refers to low-temperature growth.

Material	Buffer layer	Substrate	Growth Method	(002) FWHM (arcsec)	Reference
GaN	LT-GaN	Al_2O_3	MOCVD	220	[5]
	LT-AlN	Al_2O_3		380	[5]
	AlN/h-BN	Al_2O_3		576	[6]
	-	SiC		423	[7]
	AlN	SiC		200	[8]
	Graphene	SiC		222	[9]
	AlN/Graphene	SiC		1260	[10]
	AlN/Graphene	*SiC*		*385*	*This work*

Supplementary References

1. Dardzinski, D., Yu, M., Moayedpour, S. & Marom, N. Best practices for first-principles simulations of epitaxial inorganic interfaces. *Journal of Physics Condensed Matter* vol. 34 Preprint at https://doi.org/10.1088/1361-648X/ac577b (2022).

2. Nash, B. P. & Nash, A. The Ni-Si (Nickel-Silicon) System Equilibrium Diagram. *Bulletin of Alloy Phase Diagrams* **8**, 6–14 (1987).

3. Vojt~crtovsk', K. & Zem~ik, T. MOSSBAUER STUDY OF THE Fe-Si INTERMETALLIC COMPOUNDS. *Czechoslovak Journal of Physics B* **24**, 171–78 (1974).

4. Perring, L., Bussy, F., Gachon, J. C. & Feschotte, P. *The Ruthenium-Silicon System*. *Journal of Alloys and Compounds* vol. 284 (1999).

5. Bayram, C., Pau, J. L., McClintock, R. & Razeghi, M. Delta-doping optimization for high quality p -type GaN. *J Appl Phys* **104**, (2008).

6. Kobayashi, Y., Kumakura, K., Akasaka, T. & Makimoto, T. Layered boron nitride as a release layer for mechanical transfer of GaN-based devices. *Nature* **484**, 223–227 (2012).

7. Xie, Z. Y. *et al.* Effects of surface preparation on epitaxial GaN on 6H-SiC deposited via MOCVD. in *MRS Internet Journal of Nitride Semiconductor Research* vol. 4 (Materials Research Society, 1999).

8. Reitmeier, Z. J. *et al.* Surface and defect microstructure of GaN and AlN layers grown on hydrogen-etched 6H-SiC(0001) substrates. *Acta Mater* **58**, 2165–2175 (2010).

9. Kim, J. *et al.* Principle of direct van der Waals epitaxy of single-crystalline films on epitaxial graphene. *Nat Commun* **5**, (2014).

10. Yu, Y. *et al.* Demonstration of epitaxial growth of strain-relaxed GaN films on graphene/SiC substrates for long wavelength light-emitting diodes. *Light Sci Appl* **10**, (2021).

Other Supplementary Materials for this manuscript include:

Supplementary Video 1. AIMD simulation of the Ni/graphitic carbon/SiC system.

Supplementary Video 2. AIMD simulation of the Fe/graphitic carbon/SiC system.

Supplementary Video 3. AIMD simulation of the Ru/graphitic carbon/SiC system.